frontiers | Frontiers in Marine Science

TYPE Original Research
PUBLISHED 10 September 2025
DOI 10.3389/fmars.2025.1663981

OPEN ACCESS

EDITED BY
Tianchen He,
Hohai University, China

REVIEWED BY
Zhihui An,
Wuhan Center of China Geological Survey, China
Yisi Zhong,
Ruhr University, Germany

*CORRESPONDENCE
Anqing Chen
aqinth@163.com

RECEIVED 11 July 2025
ACCEPTED 19 August 2025
PUBLISHED 10 September 2025
CORRECTED 03 December 2025

CITATION
Wang X, Azmy K, Chen A, Sun S and Li S (2025) The resilient Middle Triassic habitable climate following Early Triassic severe carbon isotope oscillations: contributions from microbialites, Upper Yangtze Block. *Front. Mar. Sci.* 12:1663981. doi: 10.3389/fmars.2025.1663981

The resilient Middle Triassic habitable climate following Early Triassic severe carbon isotope oscillations: contributions from microbialites, Upper Yangtze Block

Xianfeng Wang[1,2], Karem Azmy[3], Anqing Chen[1,2]*, Shi Sun[1,2] and Suxiao Li[1,2]

[1]Key Laboratory of Deep-time Geography and Environment Reconstruction and Applications of Ministry of Natural Resources, Chengdu University of Technology, Chengdu, China, [2]State Key Laboratory of Oil and Gas Reservoir Geology and Exploitation, Chengdu University of Technology, Chengdu, China, [3]Department of Earth Sciences, Memorial University of Newfoundland, St. John's, NL, Canada

The Permian-Triassic mass extinction was one of the worst crises for life on earth, killing >90% of marine species, which induced the carbon cycle perturbation during the entire Early Triassic. Previous studies indicated the global CO_2 concentration dropped sharply from 2,800 ppmv to a level of approximately 450 ppmv (comparable to the present) at the Early–Middle Triassic boundary. This optimal CO_2 level, a stabilized record of 2‰ $\delta^{13}C_{carb}$, persisted throughout the Middle Triassic. While how this long-term habitable CO_2 level was maintained remains puzzling. Here, we examined the sedimentary succession that spans the duration from Late Olenekian (late Early Triassic) to Anisian (Middle Triassic), Upper Yangtze Block. The results show that the volume content of microbialites in the carbonate succession increased significantly after the transition from lower thin-bedded dolostones to upper thick-bedded microbialites, indicating the carbon pump shifted from a low-rate chemical carbonate production system to a high-rate microbial carbonate factory. The expansion of microbial mats responded to enhanced terrigenous input and elevated primary productivity. Coincidentally, the $\delta^{13}C_{carb}$ curve records a change from strong oscillations to a long-term stability. This turnover coincided with the occurrence of plant fossil assemblages (e.g., from northern Italy) and marine fossil assemblages (e.g., from South China). The findings indicate that the enhanced microbial pump, as a dynamic mechanism for atmospheric CO_2 sequestration, was a key modulator of the Middle Triassic global climate system and helped sustain more resilient ecosystems.

KEYWORDS

Middle Triassic, carbonate succession, microbialite, habitable environment, South China

1 Introduction

The Permian-Triassic mass extinction (PTME; approximately 252 Ma ago) is the cataclysmic event that led to a restructuring of marine life (Yin et al., 2001; Sahney and Benton, 2008; Alroy, 2010; Luo et al., 2010; Luo et al., 2014; Zhou et al., 2017). Following the extinction, Early Triassic ecosystems experienced a long-term stepwise rebuilding (Chen and Benton, 2012), and it was not until the early Middle Triassic epoch (Anisian) that biodiversity and complexity became comparable to those of pre-extinction faunas (Payne and Kump, 2007; Stanley, 2009; Whiteside and Ward, 2011). The plant fossil assemblages discovered in the dolostone Mountains in northern Italy during the Middle Triassic show the rich assemblages of wetland fossils and spores, indicating the extensive forest coverage and the absence of xerophytic plant groups in the setting of warm and humid land climate (Kustatscher et al., 2006; Kustatscher and Roghi, 2006; Kustatscher et al., 2010), as well as in the Luoping area of South China during Middle Triassic, marine biota fossils have been discovered, documenting a complete food chain from producers to consumers and top predators, also in response to this transition (Li et al., 2016).

It is commonly perceived that the entire Triassic environment gradually transformed from extremely warm conditions to a more habitable climate, characterized by the optimal CO_2 concentration (~400 ppmv; Korte et al., 2005; Kiessling, 2010; Luo, 2011; Luo et al., 2013). Several Early Triassic warming events were identified at the late Dienerian-Smithian boundary, in the late Smithian as well as in the late Spathian (e.g., Li et al., 2016). These warming events, accompanied by marine anoxia, ocean acidification, and enhanced weathering, were likely caused by a massive release of volcanic CO_2 (Payne et al., 2004; Li et al., 2021). The concentration of CO_2 reached 2181–2610 ppmv during the Griesbachian period in the Early Triassic and remained at 1063–1757 ppmv in the late Early Triassic. Subsequently, during the transition from the Early to Middle Triassic, the CO_2 level rapidly dropped to 343–634 ppmv (Haq et al., 1987; Li et al., 2018; Joachimski et al., 2022). Analogous trends occurred in carbon cycling (Payne and Kump, 2007; Stanley, 2009; Retallack et al., 2011; Luo et al., 2014), reflected by the multiple strong carbon-isotope oscillations (-2‰ to 5‰) during the Early Triassic. Subsequently, the $\delta^{13}C_{carb}$ component of the Anisian in the Middle Triassic gradually stabilized at 2‰ (Korngreen and Bialik, 2015). This optimal CO_2 level and Stable $\delta^{13}C_{carb}$ persisted throughout the Middle Triassic. However, the reason for the rapid drop in CO_2 levels and the long-term carbon-isotope trend remains enigmatic within the Anisian.

The vast carbonate on shallow water platforms plays a crucial role in regulating the global carbon cycle and climate change (Geyman et al., 2022). Although shallow water platforms occupy less than 10% of the global ocean area, they account for over 90% of total carbon burial in marine environments (Filbee-Dexter et al., 2024). Therefore, in the marginal sea area, marine carbonates (microbial lime muds or microbial dolostones) precipitated by microbial mediations represent a key modulator of the global climate system (e.g., Lawrence and Graham, 2012; Geyman et al., 2022). Microorganisms in the profound transition of Earth's climate during the Neoproterozoic Great Oxygenation Event and the comparable life-climate co-evolution processes in the Early Ordovician also reflect the role of regulating the climate (e.g., Trotter et al., 2008). Marine carbonates archive the geochemical variations in seawater chemistry associated with paleoenvironmental changes. Therefore, characteristics of trace element proxies reflect changes in the ancient environment, such as: bioproductivity (e.g., Ni, Zn, Cu; Wignall and Twitchett, 1996; Algeo and Maynard, 2004; Tribovillard et al., 2006; Luan et al., 2024), redox conditions (e.g., Mo, U, V, Th; Śliwiński et al., 2010; Dickson and Cohen, 2012; Tripathy et al., 2014), and climate (dry vs. wet) expressed in riverine inputs of detrital weathered material (e.g., Al, REE; Acharya et al., 2015; Moei et al., 2020; Wang and Azmy, 2020; Bian et al., 2021).

The microbialite section in the Hanwang area, located on the western margin of the Upper Yangtze Platform in South China, is characterized by a gradual transformation from thin-bedded carbonate at the bottom to microbialite at the top, thus reflecting the co-evolution of climate and life. The main objectives of the current study are: (a) To evaluate the degree of petrographic and geochemical preservation of the investigated microbialites of the Middle Triassic Leikoupo Formation in the Hanwang section; (b) To better understand the influence of Middle Anisian climate, primary productivity, and redox conditions on microbial boom during Middle Anisian; (c) To investigate the intrinsic connection between the factors maintaining the long-term optimal CO_2 level and stable carbon isotopes and the dynamic carbon sink of microorganisms during the Middle Triassic (Anisian) in South China.

2 Geological setting

The South China Block (SCB) was located in the east of the Paleo-Tethys during the Middle Triassic (Figure 1A), and this was primarily composed of the Yangtze and the Cathaysia blocks (Lehrmann et al., 2009; Zhao et al., 2013). The Southwestern part of the Upper Yangtze Plate was the Kangdian Paleo-land, which gradually transitioned to the open platform in the east (Figure 1B, Faure et al., 2016). A continuous marine carbonate succession was widely developed in the Yangtze block during the Early-Middle Triassic that transformed into terrestrial deposits in the Late Triassic (Feng et al., 1997). The Upper Yangtze Block of South China was situated at low paleolatitude during the Triassic. It consists mainly of shallow marine carbonates of a restricted platform and tidal flat sedimentary facies.

The Hanwang section (E104° 09' 48.10", N31° 27'39.14"; Figure 1C) is in Mianzhu City, Sichuan Province, China. During the Middle Triassic period, it was surrounded by Paleo-land, resulting in a relatively low sea level, restricted seawater, and weak hydrodynamic cycle conditions, which formed a semi-restricted platform environment, mainly composed of typical shallow-water sedimentary lithology such as limestone and dolostone (Huo et al., 2022). The bottom and top of the section are respectively the Jialingjiang and Tianjingshan formations, and the main part of the Hanwang section is the Leikoupo Formation (Figure 1D). There is a lithological transition from dolostones to limestone between the Leikoupo Formation and the Tianjinshan Formation. It is in parallel unconformable contact with the Jialingjiang Formation, and the boundary between the two is

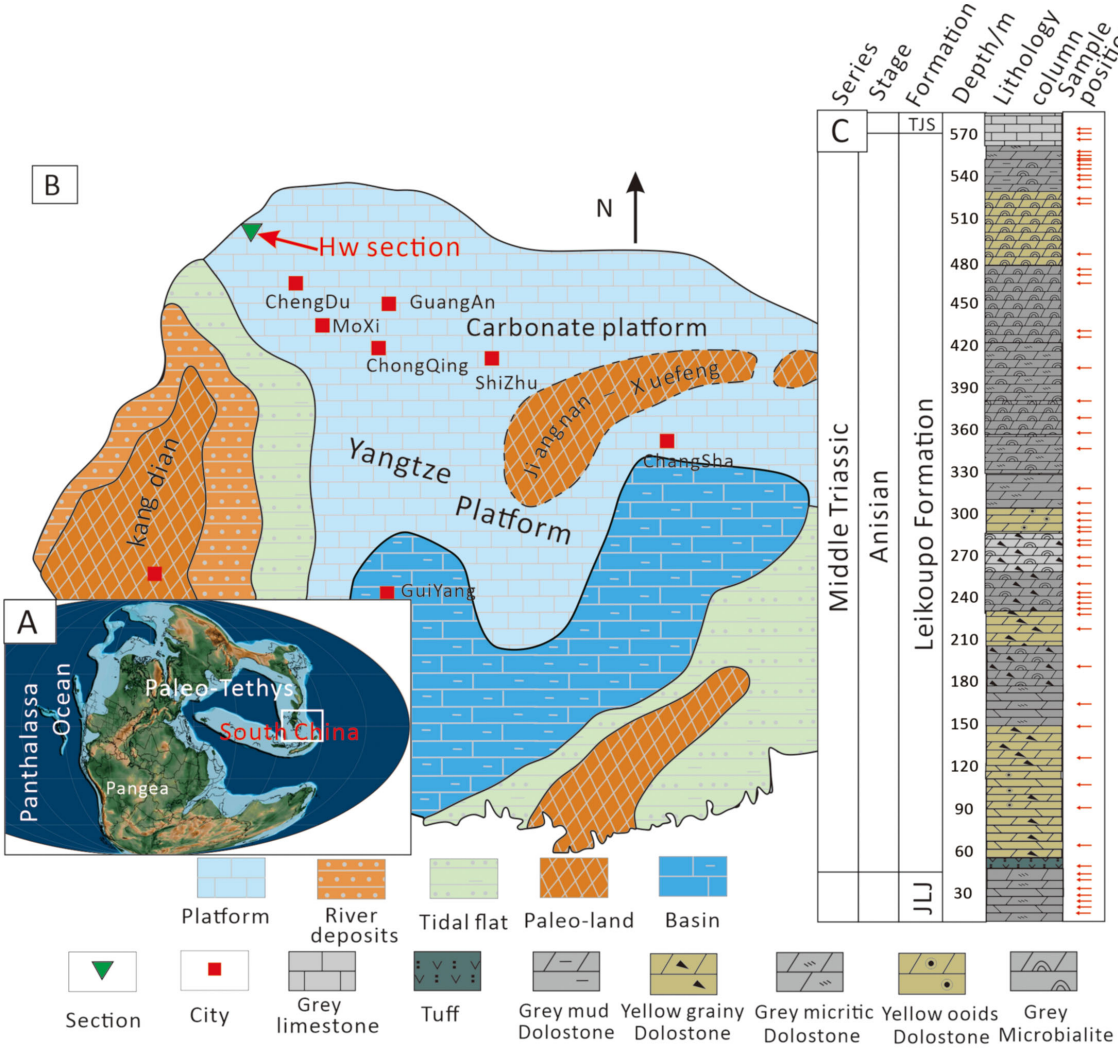

FIGURE 1
Geological background and stratigraphic column of the study area. **(A)** Paleogeographic map during the Middle Triassic (~247 Ma). Source: Map generated using GPlates software (https://www.gplates.org) and the latest pyGPlates release (v1.0.0). **(B)** Lithofacies paleogeographic map of the Middle-Upper Yangtze Platform during the Middle Triassic, showing major blocks and the approximate location of the Hanwang section (red arrow; E104°09′48.10″, N31°27′39.14″). **(C)** Stratigraphic framework of the Hanwang section showing sampling depths.

defined by the typical "Green Bean Rock", which is a widespread occurrence of volcanic tuff deposits in the early-middle Triassic boundary in South China, serving as a clear indicator of the early-middle Triassic boundary (Chen et al., 2019; He et al., 2019).

3 Samples and methods

Fifty-five fresh carbonate samples were carefully collected from the outcrop of the Leikoupo Formation and the top of the Jialingjiang Formation of the Hanwang section (Figures 1C, E 104° 09' 48.10", N31° 27' 39.14"). Thin sections (105) were cut for petrographic examination, and a clean mirror-image slab of each thin section was cleaned in a sonic bath with de-ionized water and dried to be used for geochemical sampling. Chips from the most micritic spots were ground to 200 mesh in an agate mortar, and 2 subsets were prepared for stable isotope ($\delta^{13}C_{carb}$ and $\delta^{18}O$) and elemental (major and trace element) analyses.

We quantified the proportions of microbialites components in the thin sections by dividing the field of view into regions measuring 60*45 units and identifying the microbialites components (as shown in Figure 2). Subsequently, we calculate the proportions that each component occupies within the visual field. We randomly select multiple fields of view (typically more than five) and average the calculated proportion values across these views, which ensures the randomness and reliability of the data.

Carbon and oxygen isotope compositions of 55 samples were measured at the Nanjing Hongchuang Exploration Technology Service Co., Ltd, Nanjing, China. The sample powder was reacted in an inert atmosphere with ultrapure concentrated (100%) orthophosphoric acid at 70°C in a ThermoFinnigan GasBench II. The produced gas was introduced into the IRMS (Ionic ratio mass spectrometer, MAT253) by sampling through the standard 100 µL sample loop, and CO_2 was separated from other components using a gas chromatographic column (Poraplot Q with fused silica tubing,

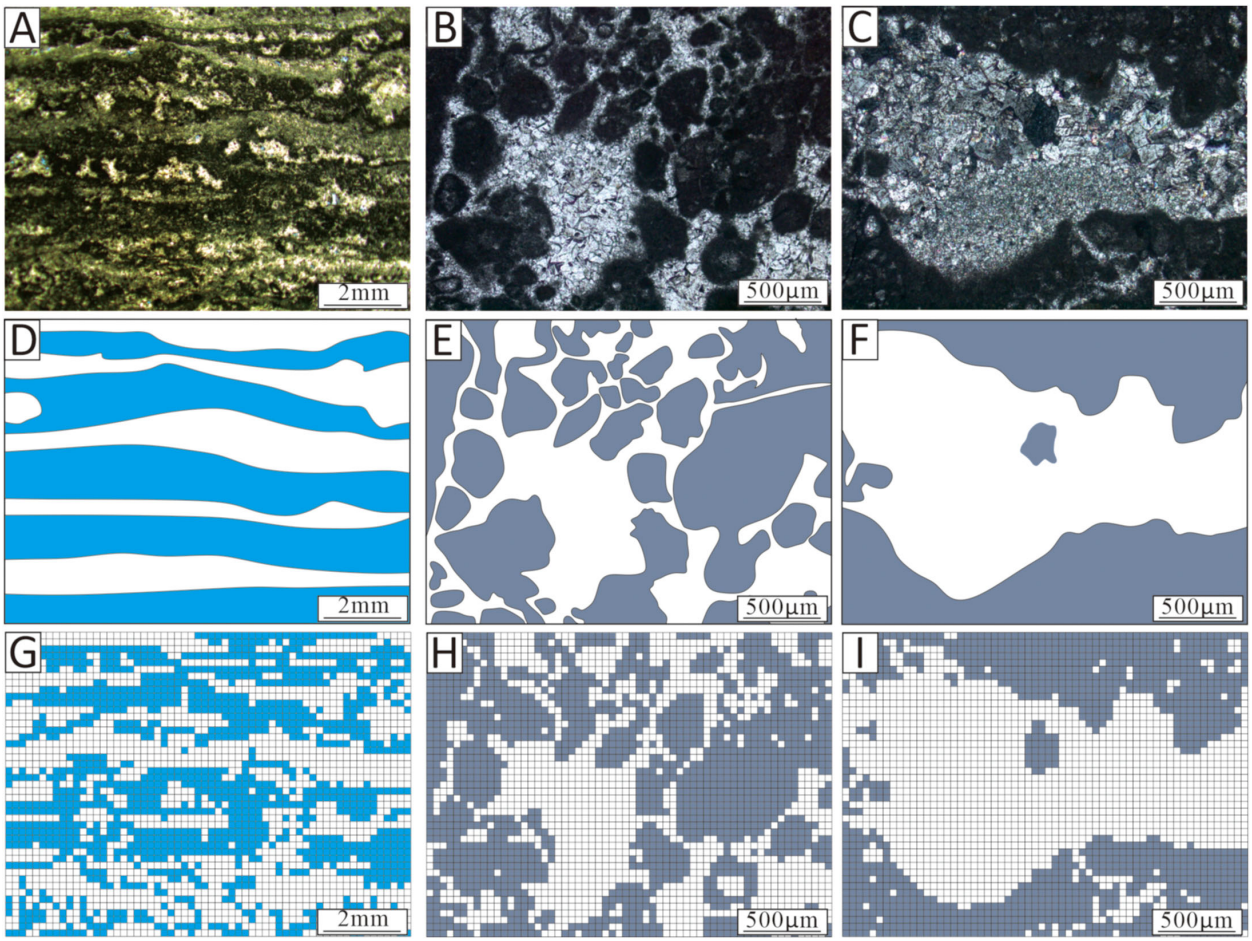

FIGURE 2
Photomicrographs of microbialites (Stromatolites in blue and Thrombolites in gray) in thin sections from the Leikoupo Formation Samples **(A)** HW36; **(B)** HW44; **(C)** HW45 showing different modes of occurrences with their sketches **(D–F)**, and biological content statistics **(G–I)**, respectively.

25m×0.32mm, Thermo Fisher Scientific), heated to 70°C. The peak corresponding to CO_2 was passed via an open split into the mass spectrometer. Isotope ratios are reported in per mil (‰) notation relative to the Vienna Pee Dee Belemnite standard (VPDB ‰). Samples were calibrated using four China standards (GBW04405, GBW04406, GBW04416, and GBW04417). The uncertainty (1σ), calculated from standards per run, is typically 0.1‰.

Major and trace elements (Appendix 1) were measured by a ZSX Primus II X-ray fluorescence spectrometer. 50 mg of the sample powder was dissolved in 1 M acetic acid in a small beaker placed in an ultrasonic water bath at 30°C for 30 min, and the solution was left at room temperature for 12h. The solution was centrifuged and washed 3 times with de-ionized water, and the residue was dried and weighed to calculate the percent of soluble material. The supernatant was then evaporated to near dryness at 120°C and redissolved in 0.2M HNO_3. The analysis process adopts China standards GBW07314, GBW07315, GBW07316, and USGS basalt standard material 6BHVO - 2 for quality control, and uncertainty was generally better than 5%.

Since analysis results are based on the total composition of the samples (carbonates and siliciclastic inclusions), the enrichment factor values of the paleoenvironmental proxies were utilized to minimize the influence of contributions from siliciclastic inclusions, in case they occur. The enrichment factor was calculated using the equation (Tribovillard et al., 2006):

$X_{EF} = [(X/Al)_{Sample}/(X/Al)_{UCC}]$ where X is the proxy element and X and Al values (in ppm) are normalized to upper crust composition (UCC; McLennan, 2001; Tribovillard et al., 2006).

4 Results

4.1 Petrography of microbialites

The basal boundary of the Leikoupo Formation is identified by the “Green Bean Rock (GBR)”, which caps the Jialingjiang Formation. The top boundary of the Leikoupo Formation is a lithological transition that is from microbial dolostone to limestone (Tianjinshan Formation). Macroscopically, the succession of the Leikoupo Formation is characterized by thin layers of dolostones in the lower part, but thick layers of microbialites in the upper part (Figure 3A).

The lower non-microbial portion is dominated by micritic dolostone beds interbedded with grainy dolostone and thin fine-grained claystone layers (Figures 3B–F). The grainy dolostones occur with horizontal bedding and cross-stratification (Figures 3C, D).

The microbialites in the upper portion of Leikoupo Formation include three types in microtexture: thrombolites, Microbial debris, and laminated stromatolite (Figures 4–6).

(1) Stromatolites: They occur as regular linear structures or the layered structure with convex-upward characteristics, alternating dark and light layers, and a thickness generally tens of centimeters (Figures 4A, B, G). The dark bands are typically organic-rich, but the lighter bands consist of trapped sediments. Based on morphology, stromatolites are classified into three fundamental types: (a) Planar stromatolites with tabular laminae (Figures 4A–C), (b) wavy Stromatolites showing sinuous undulations (Figures 4B, C), (c) domal Stromatolites characterized by convex-upward laminations (Figure 4F).

(2) Thrombolites: It is typically lack distinct structures and instead exhibit large, dark-colored clumps (Figures 5A–C). The microtexture of thrombolites occurs as narrow-laminar or pelletoid structures (with thickness< 0.1 m; Figures 5D–F), and often can be observed large numbers of tens of millimeter clots. The Thrombolites generally developed between the stromatolitic layers in the middle-Late Anisian. A few samples from the top microbialite exhibit minor recrystallization with crystals up to 70 μm (Figures 5G, H).

(3) Microbial debris: It is composed predominantly of grayish-white clumps and sand-sized particles (Figures 6A–F). Usually, obvious microbial debris and clotted structures can be observed (Figures 6B, D, F). In a few samples, due to slight recrystallization, the edges of the microbial debris structure become blurred (Figure 6A).

4.2 Evaluation of sample preservation

Diagenesis of marine carbonates significantly alters their geochemical compositions (Veizer, 1983b; Swart and Eberli, 2005; Azmy et al., 2011a). Therefore, it is crucial to evaluate their degree of petrographic and geochemical preservation. Petrographic examination has shown that the investigated carbonates are mainly dolostones with micritic (≤ 4μm) to near-micritic/microsparitic (≤ 10μm) grain size, suggesting a high degree of textural preservation and almost pristine sedimentary fabrics with insignificant recrystallization (e.g., Wang et al., 2023; Xia et al., 2023), which is consistent with a previous study (Wang et al., 2023) that proved the microbial origin of the Leikoupo Formation dolostones. However, a few samples (Figures 5G, H), with particularly high ΣREE (15–59 ppm; Figure 7; Appendix 1), show some minor recrystallization (up to 70 μm). The ΣREE values are sensitive to diagenetic alteration and increase considerably with diagenetic alteration (Azmy et al., 2015). Thus, the retention of microbial fabrics and micritic (≤ 4 μm) to near-micritic (4–10 μm) grains supports an early stage of dolomitization at the surface to near-surface conditions. The lack of evaporite interbeds (e.g., gypsum or anhydrite) in the HanWang section carbonates does not support a sabkha origin (e.g., Azmy et al., 2001), which is consistent with lower [Sr] contents of the investigated dolostones relative to those of Sabkha sediments ≥ 470 ppm (Veizer, 1983a, their table 3.3).

In addition, the molar Sr/Ca ratio of carbonates may provide clues about their parent fluids, given that the estimates of the Sr distribution coefficient (D_{Sr}=0.05–0.06) between the fluid and the precipitated dolostone have been already established (Banner, 1995) since $(^{m}Sr/^{m}Ca)_{dolostone} = D_{Sr}$ $(^{m}Sr/^{m}Ca)_{fluid}$. The estimates of the mean $(^{m}Sr/^{m}Ca)_{fluid}$ of the investigated dolostones range from 0.0039 to 0.0046, which are lower than the values of modern seawater (0.0086; Drever, 1988). Therefore, those dolostones were originally microbial lime muds that were dolomitized at early stages of diagenesis under surface conditions, likely by seawater that was mixed with meteoric waters, which agrees with the lack of evaporite interbeds and argues against a sabkha origin.

During diagenesis, the $\delta^{18}O$ values are generally depleted by water/interactions, particularly (Okafor and Azmy, 2024). However, unless there is pronounced organic matter alteration involved, the $\delta^{13}C_{carb}$ values are relatively less susceptible to diagenetic alteration (Swart, 2015) and carbonates may, therefore, retain at least their near-primary C-isotope composition. Therefore, the insignificant correlation between the $\delta^{13}C_{carb}$ and $\delta^{18}O$ values (R^2 = 0.1, Figure 7A) suggests the preservation of at least near-primary $\delta^{13}C_{carb}$ (e.g., Luan et al., 2024; Okafor and Azmy, 2024; Robacio et al., 2024). This is supported by the $\delta^{13}C_{carb}$ values of the Leikoupo Formation carbonates that fall within the range of the best-preserved Middle Triassic marine carbonates (Veizer et al., 1999). On the other hand, the $\delta^{18}O$ values are dominantly higher than those of the Middle Triassic marine carbonates (≥-2‰; Figure 7A), likely reflecting the influence of dolomitization and hot weather (Land, 1983, 1992).

The diagenetic alteration of carbonates leads to a significant decrease in their Sr contents but enrichment in other proxies such as Al, ΣREE, Mn, and Fe (Veizer, 1983b; Azmy et al., 2011b). However, the contributions from the elemental compositions of siliciclastic inclusions, particularly when using XRF analyses, may mask those from diagenesis. Therefore, correlation with the Sr/Ca ratio becomes a more reliable proxy of diagenesis since the Sr contents in siliciclastics are much lower than in those carbonates (McLennan, 2001; Luan et al., 2024). The poor correlation between the Sr/Ca and $\delta^{13}C_{carb}$ values (R^2 = 0.15; Figure 7B) supports at least near-primary $\delta^{13}C_{carb}$ signatures. The Sr/Ca ratios show insignificant correlations with the P_{org}, ΣREE, and Al (R^2 = 0.05, 0.003, 0.02, respectively; Figures 7C–E), supporting the preservation of at least near-primary signatures of those proxies that reflect ambient paleoenvironmental conditions. Diagenesis alters the contents of Sr and Mn in carbonate, and the Mn/Sr ratio is therefore used to assess the degree of diagenesis. Generally, the Mn/Sr below 10 indicates that the carbonate rock has not undergone intense alteration, and its isotopic composition can represent the original sedimentary record; the Mn/Sr below 2 suggests that the sample has well preserved the isotopic composition of the original seawater (Kaufman and Knoll, 1995), the Mn/Sr ratios of the investigated carbonates are below 2. The $\delta^{18}O$ values have to be taken with caution due to resetting by

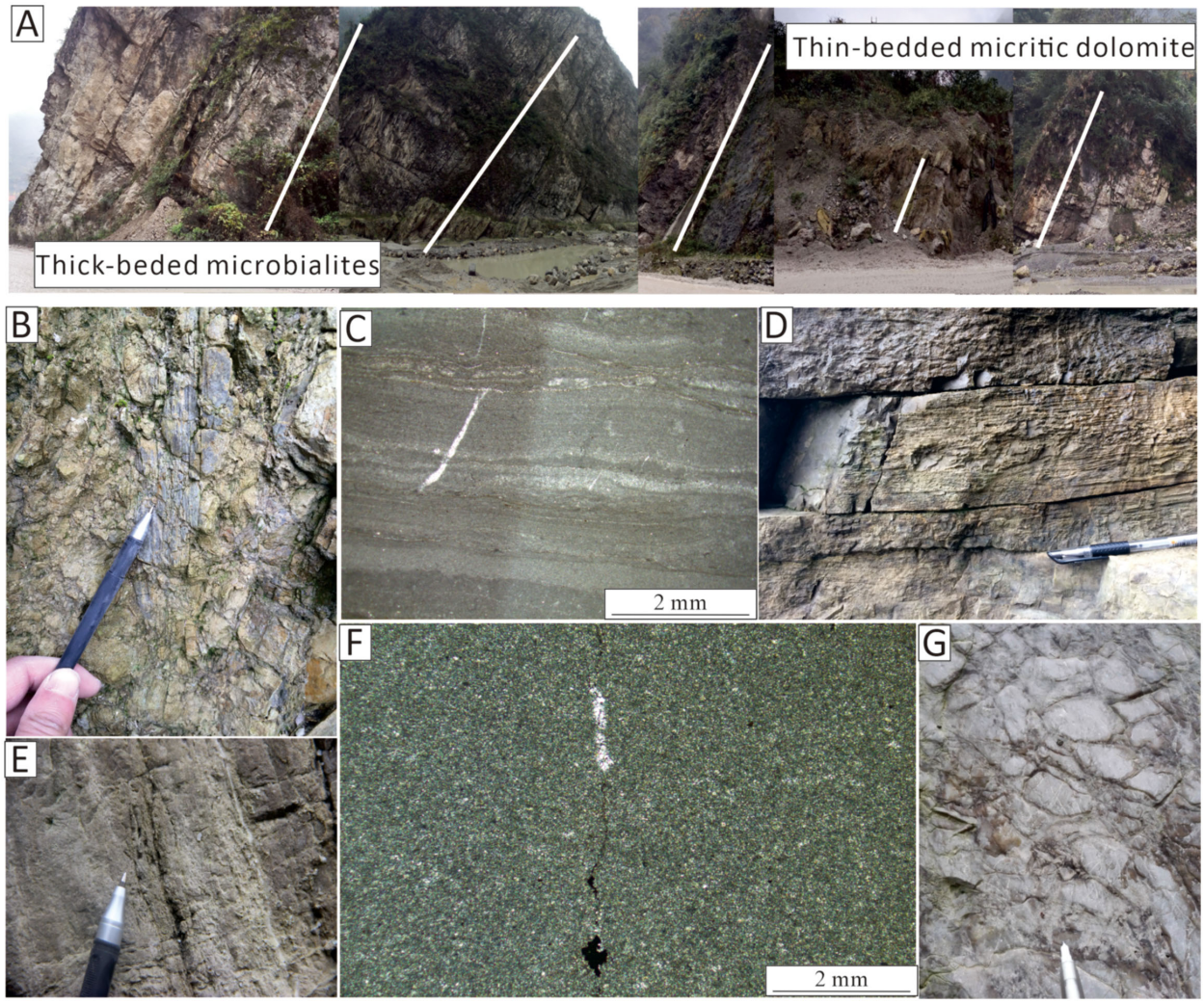

FIGURE 3
Field photographs of the Hanwang outcrop showing the features of the depositional transition from underlying thin-layered micrite dolostones to overlying thick-layered microbialites. **(A)** Panoramic macro-photos of HW sections (multiple images stitched together). **(B)** Horizontal bedding at the bottom of the Leikoupo Formation. **(C)** Micritic dolostones at approximately 160 m. **(D)** Layered structure at the bottom of the Leikoupo Formation. **(E)** Thin dolostone bed interspersed with dolomicrite at the bottom of the Leikoupo Formation. **(F)** Granular dolostone at 180 m. **(G)** Bioclastic grain-dominated dolostone at the bottom of the Leikoupo Formation.

dolomitization (Land, 1983, 1992). The Sr/Ca ratios have insignificant correlations with the Ba_{org}, Rb/Sr, Th/U, Zn, Cu, Ni, V, Mo, and Cu values (R^2 = 0.070, 0.019, 0.004, 0.006, 0.019, 0.024, 0.116, 0.007, 0.004, respectively), which suggest an insignificant impact of diagenesis on the signatures of those proxies.

4.3 Carbon isotopes and trace elements

The geochemical (isotopic and elemental) results are tabulated in Appendix 1, and their statistics are in Table 1. Based on the $\delta^{13}C_{carb}$ profile of the Leikoupo Formation (Figure 8) and transformation from dolostone to microbiolites division into 3 units. Unit 1 (~ 0–70m; $\delta^{13}C_{carb}$ = –1.8‰ to +4.2‰; Table 1) shows a distinct negative shift (~6‰). Unit2 (~ 70–330m; $\delta^{13}C_{carb}$ =+0.5‰ to +3.1‰; Table 1) exhibits a slow positive drift and Unit3 shows insignificant variations (~ 330–574m; $\delta^{13}C_{carb}$ = +1.5‰ to +2‰; Table 1).

The V_{EF} (redox proxy; Śliwiński et al., 2010; Dickson and Cohen, 2012; Tripathy et al., 2014), Th/U and Mo_{EF} values have ranges of 0.7–62.0, 0.01–1.66, and 1.2–225.3ppm, respectively. The V_{EF} profile shows a relative increase throughout Unit 2 (2.0 - 62.0 ppm; Table 1) but a decrease throughout Unit 3 (33.8 - 0.7 ppm) before an inflection near the top of Unit 3. The Mo_{EF} Profile is similar, showing an increase from 8.6 to 124.4 ppm in Unit 2 and a decrease from 225.3 - 3.7 ppm in Unit 3. On the contrary, the Th/U profile shows a negative correlation with the V_{EF} profile (Figure 8).

The P_{org}, Ba_{org}, Zn_{EF}, $Cu_{EF,}$ and Ni_{EF} values (proxies for primary productivity; e.g., Reinhard et al., 2017; Alcott et al., 2022; Robacio et al., 2024) have ranges of 19.8–247.8, 0.5–77.47, 1.0–13.2, 1.5–90.0, and 0.8–14.6, respectively (Table 1). The P_{org} profile shows minor depletion in Unit 1 (29.7 ppm; Table 1) and no

major changes in Unit 2, but there is some increase near the top of Unit 3 (19.8–247.8 ppm; Table 1). Similarly, the Ba_{org} Profile shows no major changes in Unit 2 but an increase near the top of Unit 3 (0.5–77.5 ppm; Table 1; Figure 8). The profiles of Zn_{EF}, $Ni_{EF,}$ and Cu_{EF} show the same trend, almost flat through Unit 1 but increase through Unit 2 (Table 1; Figure 5), followed by a decrease in Unit 3 except for a few peaks (Table 1; Figure 8).

The Al (200–17000 ppm; Table 1) and ∑REE (0.3–59.6 ppm; Table 1) profiles display similar patterns with high variability in Unit 1 compared to Unit 2 but a steady increase in Unit 3 (Figure 8). The Rb/Sr ratios (0.002–0.327; Table 1) are dominantly below 0.1 in Unit 2 although they are higher in Units 1 and 3 (Figure 8). The Al, ∑REE and Rb/Sr (weathering proxies) profiles show very consistent and similar trends in Units 1 and 3 compared with those in Unit 2 but the Sr/Cu (paleosalinity proxy, 9.3–117.1; Table 1) shows and opposite correlation (Figure 8). Unfortunately, measurements of other key elements such as S, B, and Ga were below method detection limits and we were unable to use them in the discussion.

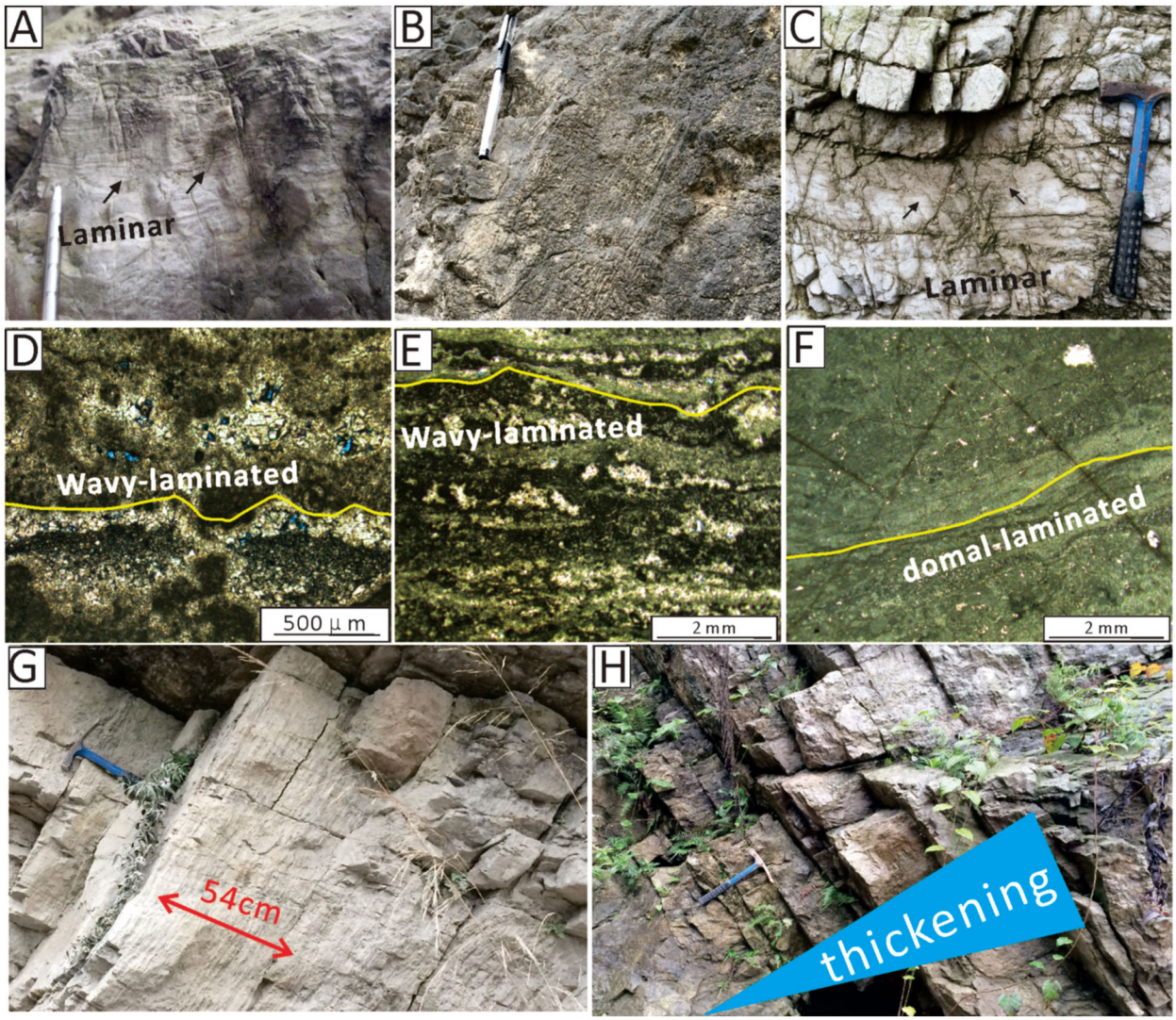

FIGURE 4
Field photographs of the stromatolite outcrops and thin-section photomicrographs of the Stromatolites. **(A)** Field photo showing domal stromatolite morphology (HW sample 540 m), interpreted as in-situ microbial buildup. Note that the black arrows indicate the laminar structure formed in the microbialites. The pen is 20 cm in length. **(B)** Stromatolite with laminar structure at approximately 517 m. **(C)** Light grey stromatolite with laminar structure in the middle of Leikoupo Formation (approximately 470 m). Note that the black arrow conveys the same meaning. **(D)** Stromatolite at approximately 420 m. Note that the yellow wavy line represents the structure of wavy-laminated. **(E)** Stromatolite at 400.15 m. Note that the yellow wavy line represents the structure of wavy-laminated. **(F)** Dark grey stromatolite at the top of the Leikoupo Formation (approximately 510 m). Note that the yellow wavy line represents the structure of a domal-laminated. **(G)** The single-layer thickness of Microbialites (approximately 500 m. The geological hammer is ~40 cm in length. **(H)** Transition from thin layer to thick layer in the middle part of the Leikoupo Formation (approximately 250 m).

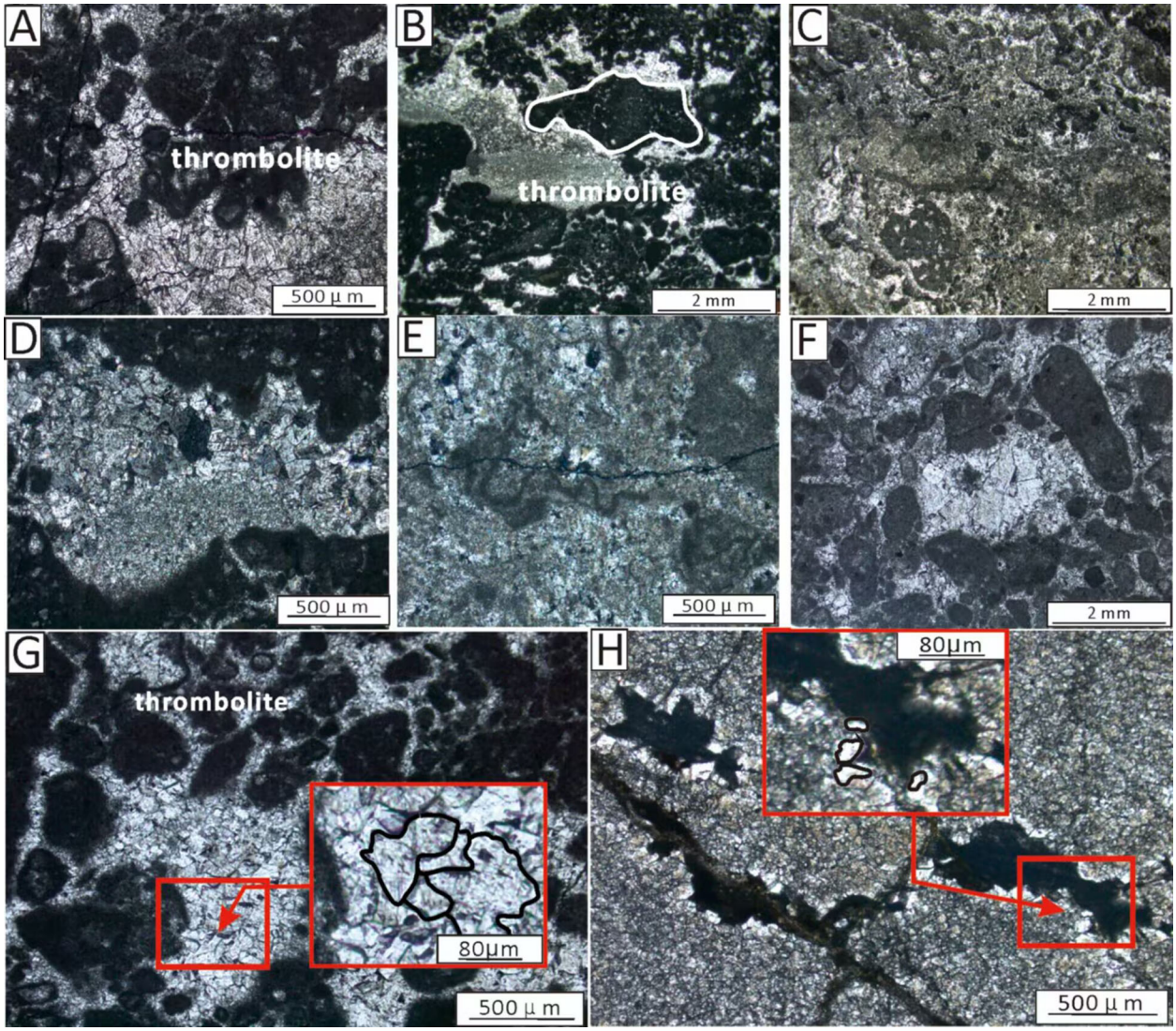

FIGURE 5
Images from thin sections of the Thrombolite. **(A)** Thrombolite at approximately 560m, **(B)** Thrombolite at approximately 547m, **(C)** Thrombolite at approximately 542m, **(D)** Thrombolite at approximately 480m, **(E)**Thrombolite at approximately 562m, **(F)** Thrombolite at approximately 540m, **(G, H)** Photomicrographs of thrombolite from Sample HW44, HW46 and their close-ups.

5 Discussion

5.1 A Middle Triassic stabilized ^{13}C platform post the late Early Triassic severe fluctuations

The Green Bean Rock (GBR), dated 247.1 to 247.3 Ma (Feng et al., 2021), is widely distributed in the Upper Yangtze, constraining the boundary between the Leikoupo and Jialingjiang formations. And the upper boundary is marked by a distinct transition to limestone. This limestone is constrained to the Ladinian (Middle Triassic) by conodont zones documented in another Hanwang section (Jin et al., 2018), thereby dating the boundary. Additionally, in the Middle-Upper Yangtze Platform, the Luolou Formation from the adjacent area represents different sedimentary facies from the same period as the Leikoupo Formation (Tong et al., 2021). The age of the Luolou Formation has been well constrained to 247.2 Ma–241.5 Ma, providing a reliable reference for correlation (Li et al., 2016). Although this dolostone succession lacks biostratigraphic controls, C-isotope stratigraphy can confine the Leikoupo Formation to the Anisian Stage (Figure 9, Li et al., 2016; Ha et al., 2019).

Aluminum and ∑REE, both enriched in crustal rocks, are used as proxies for terrigenous input into the ocean (Śliwiński et al., 2010) and are analogous to the Rb/Sr ratio due to their distinct reactivities to weathering processes (Jin et al., 2006). The Rb/Sr and ∑REE profiles show a relative enrichment in Unit 1 reflecting the enhancement of weathering that might have been associated with the mass burial of organic carbon (e.g., Yang et al., 2014, 2018). This may also explain the significant positive drift of $\delta^{13}C_{carb}$ in Unit 1 (~4‰; Figure 8) compared with the general low values (almost flat profile) throughout the overlying units. Compared with Sr

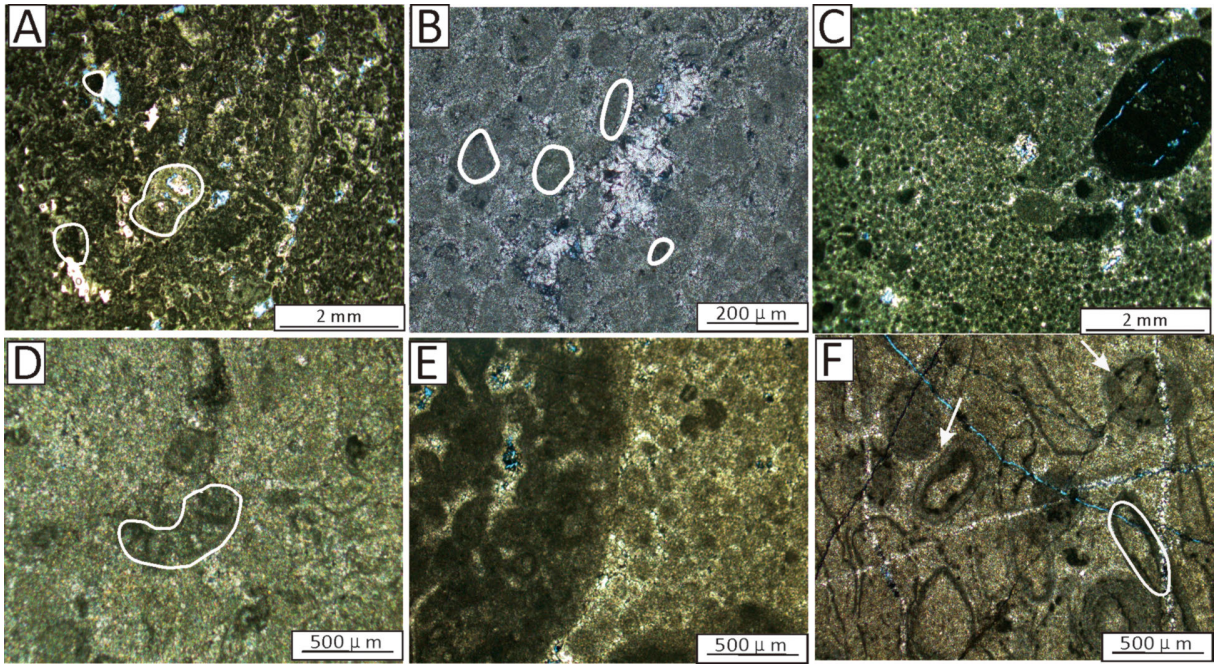

FIGURE 6
Images from thin sections of the microbial debris. **(A)** Microbialite with microbial debris at approximately 247m. Note that the white circles represent biological debris structures. **(B)** Thrombolitic boundstone at 220.15m. Note that the white circles represent clotted structures. **(C)** Microbialite with peloidal fabric at approximately 240m, **(D)** thrombolitic boundstone at approximately 245m. Note that the white circles represent biological debris structures. **(E)** Grain thrombolitic boundstone at 217m. **(F)** Microbialite with microbial debris at 240m. Note that the white circles represent biological debris structures.

(influenced by evaporation), Cu is an immobile element in sediments, and the Sr/Cu ratio is therefore utilized as a paleosalinity proxy subject to evaporation (Lerman et al., 1995). The Sr/Cu profile shows a negative correlation with the Al, ΣREE, and Rb/Sr (weathering proxies) profiles, which is consistent with a relative decrease in salinity associated with the riverine inputs of weathered material in Units 1 and 3 compared with Unit 2 (Table 1; Figure 8).

Unit 3 shows a relative decrease in the V_{EF} and Mo_{EF} values despite the relative enhancement of weathering as indicated by the Al, ΣREE, and Rb/Sr profiles (Table 1; Figure 8), thus denoting a transition towards more oxic conditions (Śliwiński et al., 2010; Dickson and Cohen, 2012). This is consistent with the correlated increase exhibited by the P_{org} and Ba_{org} (organic productivity proxies; Table 1) profiles and the general trend of decrease by the Zn_{EF}, $Cu_{EF,}$ and Ni_{EF} (micronutrient proxies) profiles (Figure 8) that may reflect a relative increase of primary productivity (Alcott et al., 2022). However, the increase in primary productivity is not correlated with a considerable stable setting on the $\delta^{13}C_{carb}$ profile, thus suggesting only a minor change likely under dysoxic rather than fully oxic conditions (e.g., Azmy et al., 2011a; Okafor and Azmy, 2024). This is consistent with the Th/U values that are entirely< 2 (boundary of anoxic/oxic conditions; Wignall et al., 2007) and barely reach ~ 1.8 in Units 1 and 3 (Figure 8).

The C-isotope fluctuation (highlighted red part in Figure 9) in HW section was followed by a $\delta^{13}C_{carb}$ long-term Middle-Triassic optimum platform period, particularly in Unit 3 (Figure 9). The same $\delta^{13}C_{carb}$ trend of the HanWang section was recorded by equivalent sections in other regions, showing that the C-isotope values remained stable at 2‰ for a long time; Figure 9, Atudorei et al., 1997; Chen and Benton, 2012; Li et al., 2016; Ha et al., 2019), which reflects a gradual attenuation of perturbations in the global carbon cycle, eventually reaching a steady state. However, considering that the changed environment will influence the isotope signatures, we must compare with different sedimentary facies in the same period. The $\delta^{13}C_{carb}$ ranges from -2‰ to 2.5‰ VPDB across the Early–Middle Triassic transition in the shallow-water Hanwang section (tidal flat) and shows higher amplitude shifts (0‰-4‰) in the deep-water Guandao section (basinal). Crucially, both sections' profiles have a stable ~2‰ during the Anisian. This synchronicity across disparate environments strongly suggests that the Anisian $\delta^{13}C_{carb}$ stability reflects a regional-to-global signal rather than local facies.

5.2 The transition from low-rate chemical to high-rate microbial carbonate factories

The lithological succession changes from the dolomicrites at the bottom to Microbialits in the middle and top. Although the sedimentological evidence indicates that the entire Hanwang section remained within a tidal flat, the Hanwang section exhibits a distinct vertical transition. The lower part of the Hanwang section shows the characteristics of the supratidal zone. It is dominated by columnar stromatolites in Unit 2, indicating adaptation to high-

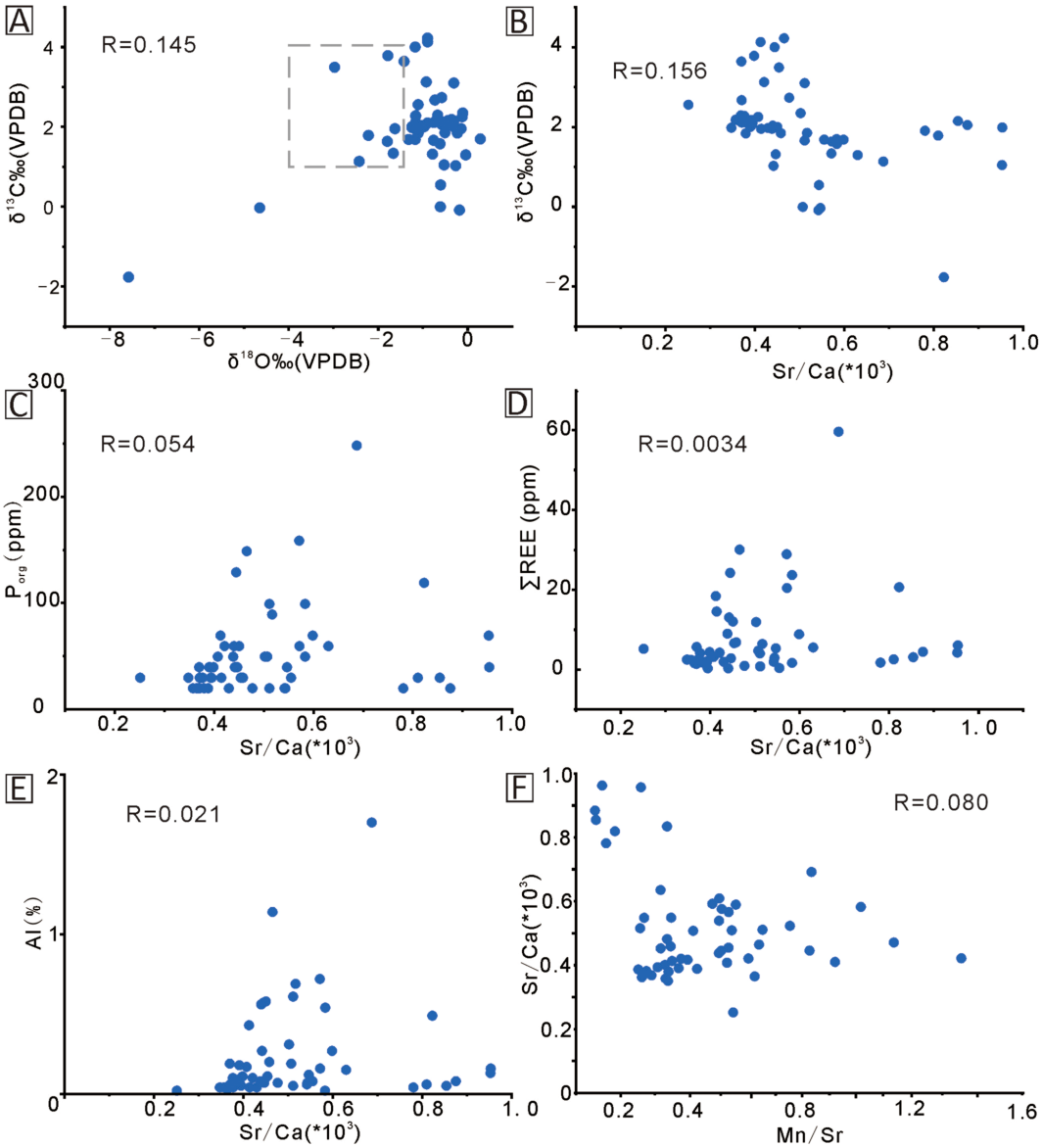

FIGURE 7
Cross-plots of **(A)** δ^{13}Ccarb versus δ^{18}O and Sr/Ca versus **(B)** δ^{13}Ccarb; **(C)** Porg; **(D)** ∑REE; **(E)** Al; and **(F)** Mn/Sr for samples from the Hw section. The square in **(A)** marks the range of composition of best-preserved Middle Triassic marine carbonates (Veizer et al., 1999).

TABLE 1 Summary of statistics of isotopic and trace element geochemical compositions of the Leikoupo Formation carbonates.

Unit	Sample ID	δ^{13}C‰ (VPDB)	Ni_{EF}	∑REE ppm	P_{org} ppm	Ba_{org} ppm	Al ppm	Rb/Sr	V_{EF}	Cu_{EF}	Zn_{EF}	Th/U	Mo_{EF}	Sr/Cu
Unit1	N	9	9	9	9	9	9	9	9	9	9	9	9	9
	Mean	2.73	1.2	13.3	74.9	14.8	3600	0.081	3.7	5.5	1.7	0.64	5.9	29.8
	Stdev	2.13	0.3	10.1	45.2	17.0	3500	0.085	2.4	2.0	0.5	0.57	6.8	15.8
	Max	4.22	1.6	30.1	148.7	51.5	11400	0.275	8.9	8.8	2.3	1.66	21.4	58.4
	Min	-1.76	0.8	4.2	29.7	0.5	1000	0.018	1.2	2.6	1.0	0.05	1.2	9.3
Unit2	N	21	21	21	21	21	21	21	21	21	21	21	21	21
	Mean	1.86	2.6	2.3	27.9	6.6	700	0.016	23.1	16.6	5.4	0.07	34.8	33.0

(Continued)

TABLE 1 Continued

Unit	Sample ID	$\delta^{13}C‰$ (VPDB)	Ni_{EF}	∑REE ppm	P_{org} ppm	Ba_{org} ppm	Al ppm	Rb/Sr	V_{EF}	Cu_{EF}	Zn_{EF}	Th/U	Mo_{EF}	Sr/Cu
	Stdev	0.79	2.8	1.8	10.0	13.4	400	0.011	15.3	8.1	2.6	0.07	26.5	12.5
	Max	3.09	14.6	9.0	49.6	56.6	1900	0.058	62.0	40.7	13.2	0.37	124.4	71.5
	Min	-0.08	1.0	0.3	19.8	0.5	300	0.006	2.0	5.2	1.2	0.02	8.6	15.3
Unit3	N	25	25	25	25	25	25	25	25	25	25	25	25	25
	Mean	1.79	2.4	10.4	63.2	12.97	3200	0.070	10.5	11.0	3.7	0.28	39.2	44.0
	Stdev	0.41	2.0	12.8	50.5	15.77	3730	0.080	11.0	17.9	3.2	0.42	47.3	31.2
	Max	2.55	11.0	59.6	247.8	77.47	17000	0.327	33.8	90.0	11.3	1.62	225.3	117.1
	Min	1.02	1.0	0.3	19.8	0.5	200	0.002	0.7	1.5	1.1	0.01	3.7	9.6

$P_{org} = [P_{sample}] - [Al_{sample} \times (P/Al)_{UCC}]$;
$Ba_{org} = [Ba_{sample}] - [Ba_{sample} \times (Ba/Al)_{UCC}]$ (e.g. Schoepfer et al., 2015).
UCC is from McLennan, 2001.

energy shallow-water conditions (likely upper intertidal to shallow subtidal) and characterized by laminar stromatolites in Unit 3, suggesting deposition in deeper, lower-energy settings (probable mid-subtidal zone; Riding, 2000). Columnar morphotypes represent a microbial strategy to resist strong hydrodynamic forces in shallow environments through vertical accretion. In contrast, laminar forms develop where reduced wave energy permits lateral microbial mat expansion, which is consistent with

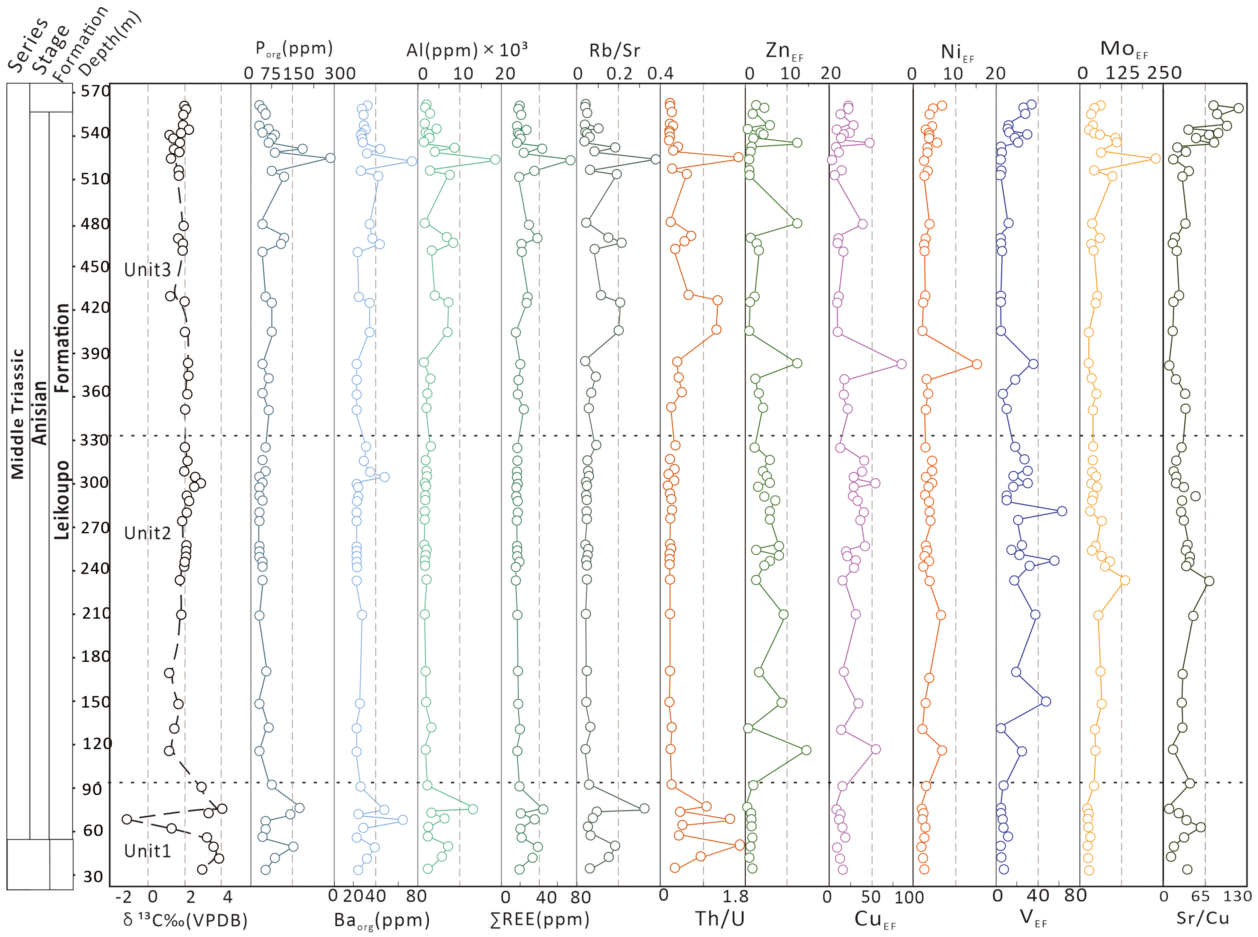

FIGURE 8
Profile of the enrichment factor of the geochemical proxies (δ^{13}Ccarb, Rb/Sr, Al, ∑REE, Ba_{org}, P_{org}, V_{EF}, Ni_{EF}, Cu_{EF}, Zn_{EF}, Th/U, Mo_{EF}, Sr/Cu) across the HanWang section.

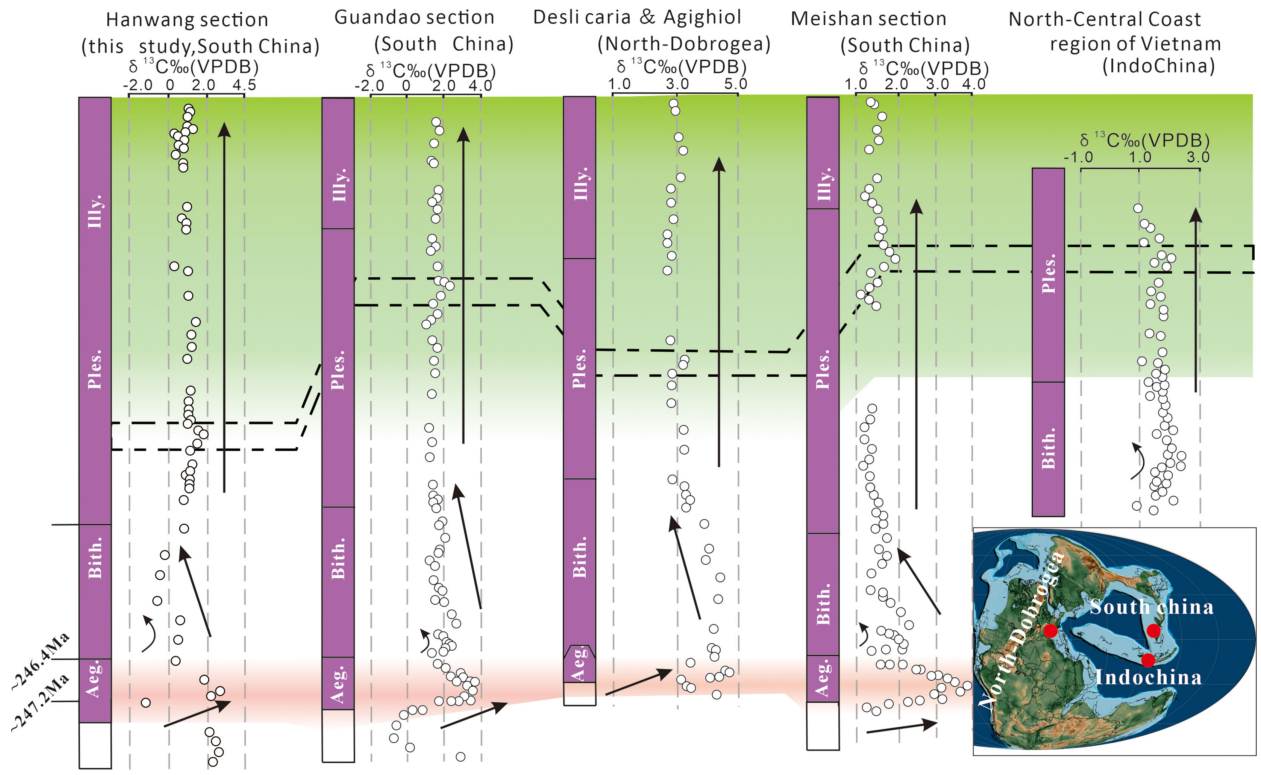

FIGURE 9
Carbon isotope stratigraphic correlations of the Leikoupo Formation in the HanWang section (this study); the Guandao section from Li et al., 2018; the North-Central Coast region of Vietnam from Ha et al., 2019; the Desli Caira and Agighiol section, North-Dobrogea from Atudorei et al., 1997; Meishan section from Chen and Benton, 2012. Source for the global paleogeographic map: As in Figure 1 (https://www.gplates.org).

regional transgressive trends during the late Anisian (e.g., Haq et al., 1987; Li et al., 2016).

The thickness of microbial beds is approximately 5 to 10 times thicker than that of thin non-microbial rocks (from 10–20 cm to 0.5 – 2 m; Figure 4G, H), which is caused by the much greater burial efficiency of CO_3^{2-} and HCO_3^- in Microbialites than in non-microbial processes (Chen et al., 2022; Boussagol et al., 2024). The considerable rise in algae photosynthetic activities enhanced carbon sinks, which influenced carbonate deposits, the burial of organic matter, as well as establishment of a microbial carbonate factory (Nédélec et al., 2007; Gérard et al., 2013). For example, cyanobacteria can accelerate the deposition of carbonate because cyanobacteria actively promote the formation of Mg-enriched microenvironment and maintain a high pH and alkalinity (predominantly CO_3^{2-} and HCO_3^-) within the sedimentary microenvironment (Nédélec et al., 2007; Gérard et al., 2013). Contemporary experiments on stromatolites also provided some supporting evidence (Gérard et al., 2013) since stromatolites can locally alkalize water, which actively promoted the establishment of carbonate rock factories and carbon burial. The structure of cyanobacterial likewise might have provided a potential capacity to construct frameworks that impeded water flow and trapped sediments, which accelerated the buildup of microbial carbonate factory (Geyman et al., 2022, Figure 10). Microbes trap and adhesion sediments *in situ*, forming thrombolite with clumpy internal characteristics and stromatolite with obvious light and dark bands (Riding, 2000; Wu et al., 2014; Figure 10) to develop layers of Microbialites.

Following the estimation by Shen et al. (2015) based on Milankovitch cycle analysis, the carbonate deposition rates in shallow-water regions dominated by microbialites are relatively high, with a mean value of 23 cm/kyr. This is consistent with our data from the Hanwang section, where approximately 250 meters of Microbialites intervals were deposited within ~1.5 Ma after the Pelsonian Humid Event. In contrast, the carbonate deposition rate of non-microbialites in the lower part of the Leikoupo Formation is approximately 10.0 cm/kyr, and the deposition rate of non-microbialites at the top of the Jialingjiang Formation is only 4.6 cm/kyr. Following the Mid-Anisian, the increase in sediment flux and the exponential thickening of microbial carbonate layers served as evidence for the indispensable role of microorganisms in carbon sequestration (Chen et al., 2022, Wu et al., 2014), which implies that the carbon sequestration by microorganisms (Chen et al., 2022) might have contributed to the acceleration of carbon burial and onset of a habitable climate.

5.3 A long-term habitable climate linked to microbial boom during the Middle Triassic

The climatic background of the Early Triassic was characterized by multiple high-temperature events that led to a slow recovery of life (Retallack et al., 2011; Luo et al., 2010, 2013, and 2014; Song et al., 2015; Li et al., 2016; Cavicchioli et al., 2019). Among these, the last extreme event occurred at the Anisian-Olenekian boundary (OAB event),

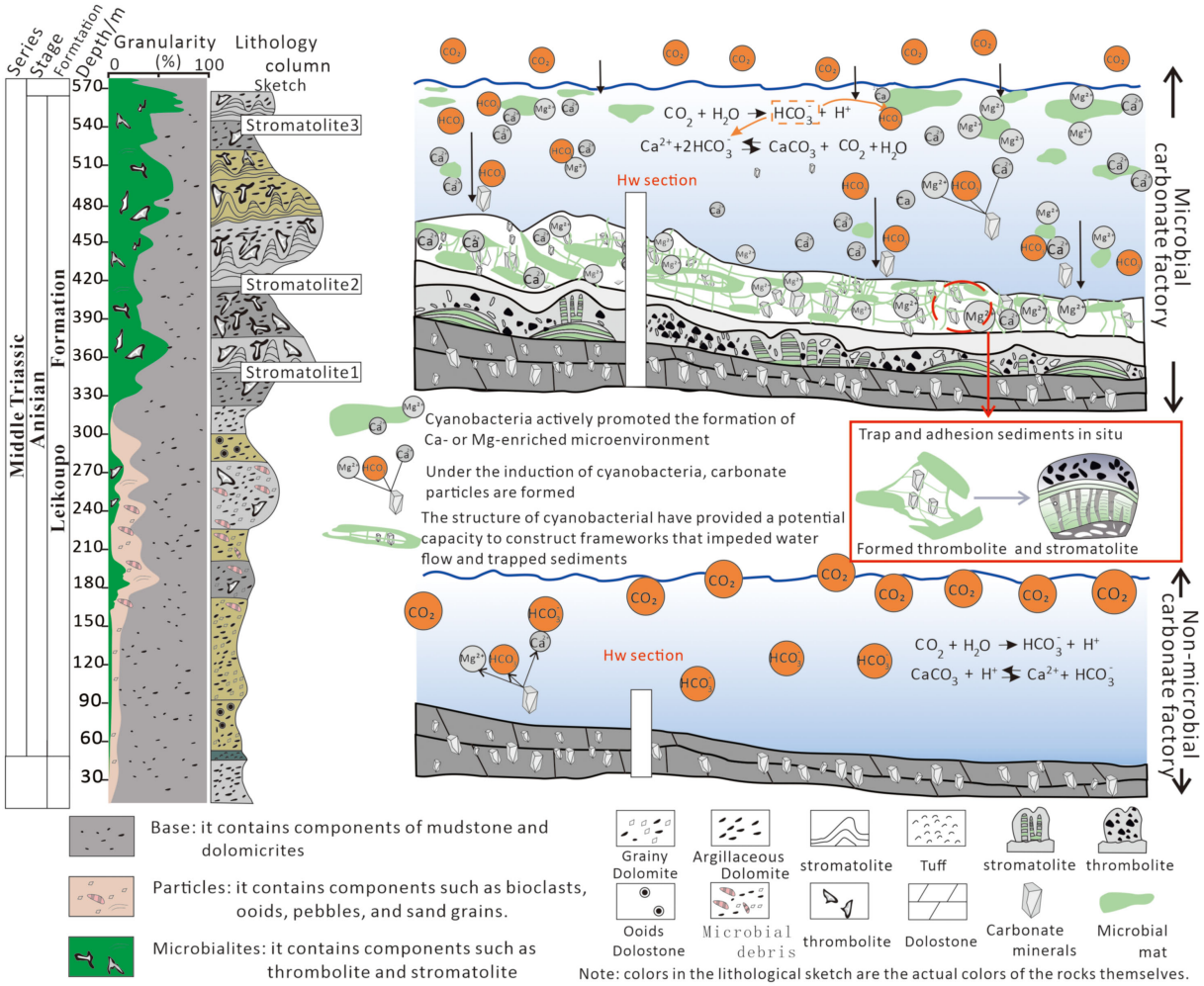

FIGURE 10
Expansion of microbialites and changes in carbonate factories from the late Early Triassic to the Middle Triassic, as well as the pattern diagram of the formation of stromatolites and thrombolites promoted by microorganisms. Source: Pattern diagram adapted from Boussagol et al. (2024), published under CC BY NC ND 4.0 License.

which caused high temperatures as documented by the $\delta^{18}O_{apatite}$ (Sun et al., 2012), ocean hypoxia (Zhou et al., 2017), and acidification (Figure 11; Song et al., 2015; Feng et al., 2021). During the C-isotope negative drift event of the Late Olenekian, the $\delta^{13}C_{carb}$ values of the best-preserved marine carbonates worldwide were recorded as close to −2‰ VPDB (shown as the red highlighted part in Figure 9; Veizer et al., 1999), which is attributed to contributions from the light CO_2 associated with the large volcanic eruptions around the latest Permian-Early Triassic time interval (Feng et al., 2021; Li et al., 2018). Subsequently, the temperature began to decline gradually, a process that lasted approximately 5 Ma, and the climate and environment gradually transitioned to more habitable conditions. At this stage, the synchronous decrease in $^{87}Sr/^{86}Sr$ ratios with pCO_2 (Veizer et al., 1999; Hu et al., 2008; Brand et al., 2010; Joachimskil et al., 2022) suggests that the enhanced weathering can explain the cooling trend (Figure 11), as the weathering of silicic rocks consumed CO_2 and contributed to a decrease in temperature (e.g., Yang et al., 2014, 2018).

Life evolution also responded to that shift towards more habitable conditions. Evidence includes the recovery of reefs and Dasyclad algae (Flügel, 2002; Payne et al., 2004), the discovery of the complete marine biological fossils in Luoping (Benton et al., 2013; Li et al., 2018), the discovery of complete plant fossils in the dolostone Mountains of northern Italy (Kustatscher et al., 2006; Kustatscher and Roghi, 2006; Kustatscher et al., 2010), as well as the abundant hygrophytic paleobotanical and palynological assemblages (Figure 11; Hermann et al., 2012; Retallack, 2013). Coincidentally, the investigated dolostones of the HanWang section also document a rapid shift from thin micrite carbonate to thick microbialites during this crucial transition period (Figure 11). The same situation occurred in other low-latitude regions during the Middle Triassic. For instance, sedimentary records of stromatolites have been documented in places such as the German Basin, California, Greenland, and the Yunnan Province, South China (e.g., Luo et al., 2014; Pei et al., 2022; Huang et al., 2022; Palaeogeographical map in Figure 11).

The global paleoclimate records also revealed a transient wet phase during the Pelsonian substage (~244.3 Ma; Middle Anisian; Figure 11; Stefani et al., 2010; Sun et al., 2012). The warm and humid

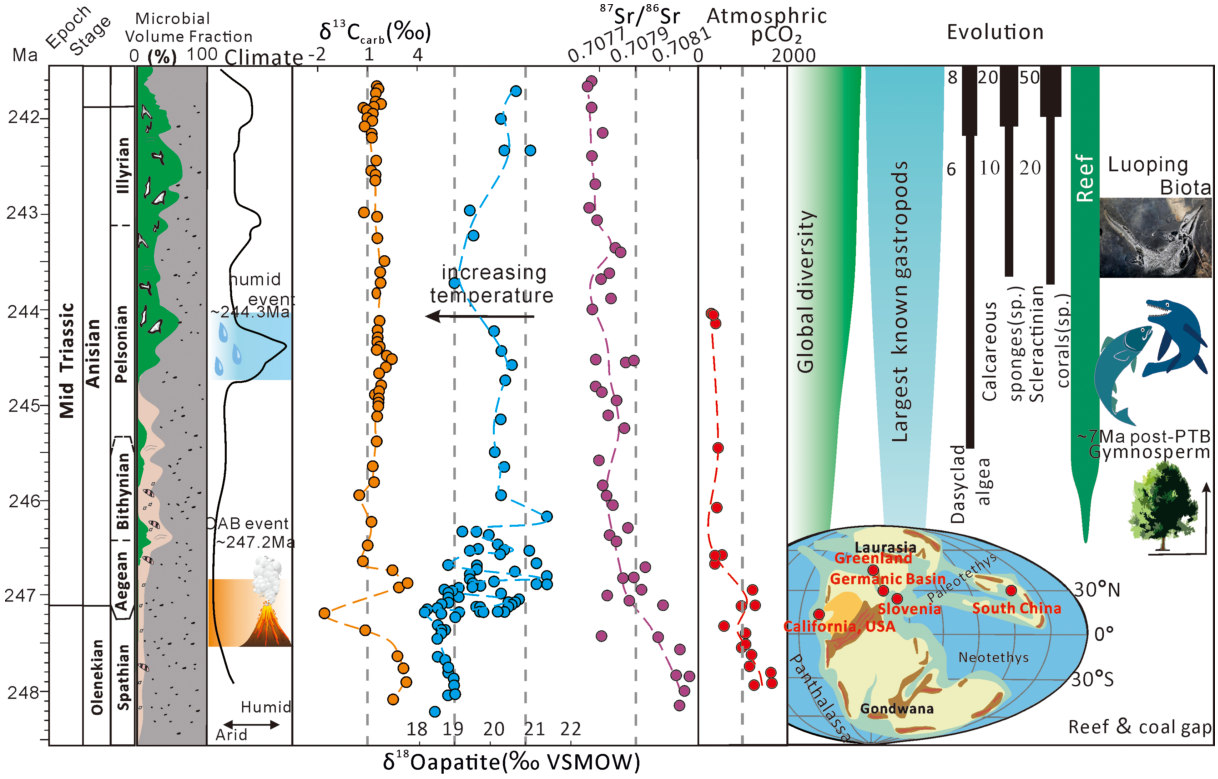

FIGURE 11
The expansion of the microbial carbon sink coincided with the stabilization of the Middle Triassic climate and the recovery of Earth's ecosystems. The $\delta^{13}C_{carb}$ is from this study; $\delta^{18}O_{apatite}$ is from Li et al. (2018); Luoping faunas are from Benton et al. (2013); Reef, Global Diversity, Largest known gastropods and Dasyclad algae are from Flügel (2002) and Payne et al. (2004); Calcareous sponges and Scleractinian corals are from Kiessling, (2010); Reconstruction of atmosphere pCO_2 is from Joachimski et al. (2022); Climate is from Stefani et al. (2010). Source for the global paleogeographic map: As in Figure 1 (https://www.gplates.org).

climate further enhances the abundance of surface runoff and the intensity of chemical weathering. The weathered organic matter from terrestrial sources, particularly in warm conditions and high salinity, decreases the solubility of O_2 in water (e.g., Li et al., 2020; Zhu et al., 2023; Okafor and Azmy, 2024; Robacio et al., 2024), and converts phosphorus-containing rock minerals into soluble phosphates (such as $H_2PO_4^-$, HPO_4^{2-}) that are carried away by rainwater and surface runoff to the ocean. The increase in P_{org} inputs is documented in Middle-Late Anisian (similar evidence also recorded in Unit 3 of the Hanwang section). A considerable rise in oceanic primary productivity further fostered a flourishing of microorganisms that increased carbon sink activity. Meanwhile, enhanced weathering during the Middle Anisian stage provided Ca^{2+} and HCO_3^- to the microbial carbonate factory. This elevated production and accumulation of carbonates and enhanced lithification. These processes collectively exerted an advantageous influence on the establishment of carbonate platforms (Reinhard et al., 2017), resulting in the establishment of a microbial carbonate factory increased the rate of carbonate production and accelerated carbon burial and the formation of habitable environments. These changes synchronized with the restoration of Middle Triassic terrestrial ecosystems. It means that Microbial carbon sinks can sequester atmospheric CO_2 and more resilient burial of ^{12}C, contributing to the persistence of the long-term optimal CO_2 level and Stable $\delta^{13}C_{carb}$ during the entire Middle Triassic.

6 Conclusion

1. The Leikoupo Formation carbonates of the HanWang section span the entire Anisian (Middle Triassic) in the southwest of the Upper Yangtze. Lithofacies and petrographic examinations reveal a transition from thin layers of dolomicrites to thicker microbialites, suggesting a microorganism-mediated origin that enhanced the thickness.
2. The profiles of proxies such as those of terrigenous inputs (Rb/Sr, ΣREE, and Al), paleo-redox conditions (Th/U, V_{EF}, Mo_{EF}), and primary productivity (P_{org}, Ba_{org}, Zn_{EF}, Cu_{EF}, Ni_{EF}) show drastic changes in conditions during the Late Olenekian. The climate conditions during the middle-late Anisian were generally stable, with a biologically habitable background characterized by a recovery in terrigenous input and primary productivity. The recovery of paleoenvironmental conditions is consistent with the transition of the carbonate lithofacies temporally, indicating environmental revival closely intertwined with the establishment of a microbial carbonate factory.
3. The variations of proxy profiles across the investigated HanWang section support critical changes in global sea level, paleotemperature, atmosphere pCO_2, paleoclimate, and biological evolution, as well as the global $\delta^{13}C_{carb}$ that led to

globally suitable, stable greenhouse climate and played a significant role in the reproduction, development of organisms, and the establishment of ecosystems during the Anisian. The Pelsonian substage is a crucial time for biological recovery, and the low-latitude microbial carbon sinks may be an important factor in maintaining a resilient habitable climate.

Data availability statement

The original contributions presented in the study are included in the article/Supplementary Material. Further inquiries can be directed to the corresponding author/s.

Author contributions

XW: Conceptualization, Data curation, Formal Analysis, Investigation, Methodology, Writing – original draft. KA: Validation, Visualization, Writing – review & editing. AC: Conceptualization, Funding acquisition, Resources, Supervision, Writing – review & editing. SS: Data curation, Formal Analysis, Writing – review & editing. SL: Data curation, Formal Analysis, Writing – review & editing

Funding

The author(s) declare that financial support was received for the research and/or publication of this article. We thank anonymous reviewers for their constructive reviews. We thank Wenpeng Xia for his valuable and constructive suggestions during this research. This work was supported by the National Natural Science Foundation of China (Grant No. U24A20591, 42402120, 42272132), Sichuan Science and Technology Program (2023NSFSC1986), and the Everest Scientific Research Program of Chengdu University of Technology (Grant No.2025ZF11402).

Conflict of interest

The authors declare that the research was conducted in the absence of any commercial or financial relationships that could be construed as a potential conflict of interest.

Correction note

12 November 2025 A correction has been made to this article. Details can be found at: 10.3389/fmars.2025.1703935.

03 December 2025 This article has been corrected with minor changes. These changes do not impact the scientific content of the article.

Generative AI statement

The author(s) declare that no Generative AI was used in the creation of this manuscript.

Any alternative text (alt text) provided alongside figures in this article has been generated by Frontiers with the support of artificial intelligence and reasonable efforts have been made to ensure accuracy, including review by the authors wherever possible. If you identify any issues, please contact us.

Publisher's note

Supplementary material

The Supplementary Material for this article can be found online at: https://www.frontiersin.org/articles/10.3389/fmars.2025.1663981/full#supplementary-material

References

Acharya, S. S., Panigrahi, M. K., Gupta, A. K., and Tripathy, S. (2015). Response of trace metal redox proxies in continental shelf environment: the Eastern Arabian Sea scenario. *Continent. Shelf Res.* 106, 70–84. doi: 10.1016/j.csr.2015.07.008

Alcott, L. J., Mills, B. J. W., Bekker, A. S., Bekker, A., and Poulton, S. W. (2022). Earth's great oxidation event facilitated by the rise of sedimentary phosphorus recycling. *Nat. Geosci.* 15, 210–215. doi: 10.1038/s41561-022-00906-5

Algeo, T. J., and Maynard, J. B. (2004). Trace element behavior and redox facies in core shales of Upper Pennsylvanian Kansas-type cyclothems. *Chem. Geol.* 206, 289–318. doi: 10.1016/j.chemgeo.2003.12.009

Alroy, J. (2010). The shifting balance of diversity among major marine animal groups. *Science* 329, 1191–1194. doi: 10.1126/science.1189910

Atudorei, V., Baud, A., Crasquin-Soleau, S., Galbrun, B., Gradinaru, E., Mirauta, E., et al. (1997). "Extended scientific report of the Peri," in *Tethys project "The triassic of north dobrogea"*. (Lausanne: Geological Museum, Lausanne).

Azmy, K., Brand, U., Sylvester, P., Gleeson, S., Logan, A., Bitner, M. A., et al. (2011a). Biogenic and abiogenic low-Mg calcite (bLMC and aLMC): evaluation of seawater-REE composition, water masses and carbonate diagenesis. *Chem. Geology.* 280, 180–190. doi: 10.1016/j.chemgeo.2010.11.007

Azmy, K., Kendakk, K., Brand, U., Stouge, S., and Gordon, G. W. (2015). Redox conditions across the Cambrian-Ordovician boundary: Elemental and isotopic signatures retained in the GSSP carbonates. *Palaeogeogr. Palaeoclimatol. Palaeoecol.* 440, 440–445. doi: 10.1016/j.palaeo.2015.09.014

Azmy, K., Lavoie, D., Wang, Z. R., Brand, U., Al-Aasm, I., Jackson, S., et al. (2011b). Magnesium-isotope and REE compositions of Lower Ordovician carbonates from eastern Laurentia: Implications for the origin of dolostones and limestones. *Chem. Geology.* 356, 64–75. doi: 10.1016/j.chemgeo.2013.07.015

Azmy, K., Veizer, J., Misi, A., de Oliveira, T. F., Sanches, A. L., and Dardenne, M. A. (2001). Dolomitization and isotope stratigraphy of the Vazante formation, São Francisco Basin, Brazil. *Precambrian Res.* 112, 303–329. doi: 10.1016/S0301-9268(01)00194-2

Banner, J. L. (1995). Application of the trace element and isotope geochemistry of strontium to studies of carbonate diagenesis:Sedimentology. *Sedimentology* 42, 805–824. doi: 10.1111/j.1365-3091.1995.tb00410.x

Benton, M. J., Zhang, Q., Hu, S., Chen, Z. Q., Wen, W., Liu, J., et al. (2013). Exceptional vertebrate biotas from the Triassic of China, and the expansion of marine ecosystems after the Permo-Triassic mass extinction. *Earth-Science Rev.* 125, 199–243. doi: 10.1016/j.earscirev.2013.05.014

Bian, L., Schovsbo, N. H., Chappaz, A., Zheng, X., Nielsen, A. T., Ulrich, T., et al. (2021). Molybdenum-uranium vanadium geochemistry in the lower Paleozoic Alum Shale of Scandinavia: Implications for vanadium exploration. *Int. J. Coal Geol.* 239, 103730. doi: 10.1016/j.coal.2021.103730

Boussagol, P., Vennin, E., Monna, F., Millet, L., Bonnotte, A., Motreuil, S., et al. (2024). Carbonate mud production in lakes is driven by degradation of microbial substances. *Commun. Earth Environ.* 5, 533. doi: 10.1038/s43247-024-01709-9

Brand, U., Azmy, K., Tazawa, J. I., Sano, H., and Buhl, D. (2010). Hydrothermal diagenesis of Paleozoic seamount carbonate components. *Chem. Geology* 278, 173–185. doi: 10.1016/j.chemgeo.2010.09.010

Cavicchioli, R., Ripple, W. J., Timmis, K. N., Azam, F., Bakken, L. R., Baylis, M., et al. (2019). Scientists' warning to humanity: microorganisms and climate change. *Nat. Rev. Microbiol.* 17, 569–586. doi: 10.1038/s41579-019-0222-5

Chen, Z. Q., and Benton, M. J. (2012). The timing and pattern of biotic recovery following the end-Permian mass extinction. *Nat. Geosci.* 5, 375–383. doi: 10.1038/ngeo1475

Chen, Z. Q., Fang, Y. H., Wignall, P. B., Guo, Z., Wu, S. Q., Liu, Z. L., et al. (2022). Microbial blooms triggered pyrite framboid enrichment and oxygen depletion in carbonate platforms immediately after the latest Permian extinction. *Geophysical Res. Lett.* 49. doi: 10.1029/2021GL096998

Chen, A. Q., Yang, S., and Xu, S. L. (2019). Sedimentary model of marine evaporites and implications for potash deposits exploration in China. *Carbonates Evaporites* 34, 83–99. doi: 10.1007/s13146-018-0443-0

Dickson, A. J., and Cohen, A. S. (2012). A molybdenum isotope record of Eocene thermal maximun 2: Implications for global ocean redox during the early Eocene. *Paleoceanography* 27, 3230. doi: 10.1029/2012PA00234610.1029/2012PA002346

Drever, J. I. (1988). *The geochemistry of natural waters: Surface and groundwater environments. 3d* (Englewood Cliffs, New Jersey, Prentice-Hall), 437.

Faure, M., Lin, W., Chu, Y., and Lepvirier, C. (2016). Triassic tectonics of the southern margin of the South China Block. *Comptes Rendus Geosci.* 348, 5–14. doi: 10.1016/j.crte.2015.06.012

Feng, Z. Z., Bao, Z. D., Wu, S. H., Li, Y. T., and Wang, G. L. (1997). *Lithofacies paleogeography of early and middle Triassic of South China* (Beijing: Petroleum Industry Press).

Feng, M. S., Meng, W. B., Zhang, C. G., Zhang, C. G., Qing, H. R., Chi, G. X., et al. (2021). Geochronology and geochemistry of the "green-bean rock" (GBR, a potassium-rich felsic tuff) in the western margin of the Yangtze platform, SW China: Significance for the Olenekian-Anisian boundary and the Paleo-Tethys tectonics. *Lithos* 382, 383. doi: 10.1016/j.lithos.2020.105922

Filbee-Dexter, K., Pessarrodona, A., Pedersen, M. F., Wernberg, T., Duarte, C. M., Assis, J., et al. (2024). Carbon export from seaweed forests to deep ocean sinks: Nature Geoscience. *Nature Geoscience* 17, 552–559. doi: 10.1038/s41561-024-01449-7

Flügel, E. (2002). Triassic reef patterns. *Phanerozoic Reef Patterns* 72, 391–464.

Gérard, E., Ménez, B., Couradeau, E., Moreira, D., Benzerara, K., Tavera, R., et al. (2013). Specific carbonate-microbe interactions in the modern microbialites of Lake Alchichica (Mexico). *ISME J.* 7, 1997–2009.

Geyman, E. C., Wu, Z., Nadeau, M. D., Edmonsond, S., Turner, A., Purkis, S. J., et al. (2022). The origin of carbonate mud and implications for global climate. *Proc. National. Acad. Sci.* 119, e2210617119. doi: 10.1073/pnas.2210617119

Ha, T. T. N., Takayanagi, H., Ueno, K., Asahara, Y., Yamamoto, K., Iryu, Y., et al. (2019). Litho-, bio-, and chemostratigraphy of the Middle Triassic carbonate succession in the North-Central Coast Region of Vietnam. *Earth Planetary Sci.* 6, 47. doi: 10.1186/s40645-019-0293-y

Haq, B. U., Jan, H., and Vail, P. R. (1987). Chronology of fluctuating sea levels since the Triassic. *Science* 235, 1156–1167. doi: 10.1126/science.235.4793.1156

He, D. F., Ma, Y. S., Li, Y. Q., and S., L. (2019). New directions in an established gas play: promising dolostone reservoirs in the Middle Triassic Leikoupo Formation of the Sichuan Basin, China. *AAPG Bull.* 103, 1–29. doi: 10.1306/05111816502

Hermann, E. S., Hochuli, P. A., Bucher, H., Goudemand, N., Brühwiler, T., and Galfetti, T. (2012). Palynology of the Lower Triassic succession of Tulong, South Tibet — Evidence for early recovery of gymnosperms. *Palaeogeogr. Palaeoclimatol. Palaeoecol* v.339–341, 339–341, 12 – 24. doi: 10.1016/j.palaeo.2012.04.010

Hu, Z. W., Huang, S. J., Qing, H. R., Wang, Q. D., Wang, C. M., Gao, X. Y., et al. (2008). Evolution and global correlation for strontium isotopic composition of marine Triassic from Huaying Mountains, eastern Sichuan, China. *Sci. China Ser. D: Earth Sci.* 51, 540–549. doi: 10.1007/s11430-008-0031-6

Huang, Y., Chen, Z. Q., Wu, S., and Feng, X. (2022). Anisian (Middle Triassic) stromatolites from Southwest China: Biogeological features and implications for variations of filament size and diversity of Triassic cyanobacteria. *Palaeogeography Palaeoclimatology Palaeoecol.* 601, 111150. doi: 10.1016/j.palaeo.2022.111150

Huo, F., Wen, H. G., Li, L., Luo, B., Zhou, G., Xu, W. L., et al. (2022). Influence of the depositional environment on the formation of organic-rich marine shale: A case study of the first discovery of Anisian shale in the Sichuan Basin. *J. Petroleum Sci. Eng.* 214, 110577. doi: 10.1016/j.petrol.2022.110577

Jin, Z., Cao, J., Wu, J., and Wang, S. (2006). A Rb/Sr record of catchment weathering response to Holocene climate change in Inner Mongolia. *Earth Surface Processes Landforms* 31, 285–291. doi: 10.1002/esp.1243

Jin, X., Shi, Z., Rigo, M., et al. (2018). Carbonate platform crisis in the Carnian (Late Triassic) of Hanwang (Sichuan Basin, South China): Insights from conodonts and stable isotope data. *J. Asian Earth Sci.* 164, 104–124. doi: 10.1016/j.jseaes.2018.06.021

Joachimski, M. M., Müller, J., Gallagher, T. M., Mathes, G., Chu, D. L., Mouraviev, F., et al. (2022). Five million years of high atmospheric CO2 in the aftermath of the Permian-Triassic mass extinction. *Geology* 50, 650–654. doi: 10.1130/G49714.1

Kaufman, A., and Knoll, A. (1995). Neoproterozoic variations in the C-isotopic composition of seawater: stratigraphic and biogeochemical implications. *Precambrian Res.* 73, 27–49. doi: 10.1016/0301-9268(94)00070-8

Kiessling, W. (2010). Reef expansion during the Triassic: spread of photosymbiosis balancing Climatic cooling. *Palaeogeography Palaeoclimatology Palaeoecol.* 290, 11–19. doi: 10.1016/j.palaeo.2009.03.020

Kiessling, W., Flügel, E., and Golonka, J. (2002). Phanerozoic reef patterns. *SEPM Soc. Sedimentary Geology* 72. doi: 10.2110/pec.02.72

Korngreen, D., and Bialik, O. M. (2015). The characteristics of carbonate system recovery during a relatively dry event in a mixed carbonate/siliciclastic environment in the Pelsonian (Middle Triassic) proximal marginal marine basins: a case study from the tropical Tethyan northwest Gondwana margins. *Palaeogeography Palaeoclimatology Palaeoecol.* 440, 793–812. doi: 10.1016/j.palaeo.2015.09.026

Korte, C., Kozur, H. W., and Veizer, J. (2005). δ13C and δ18O values of Triassic brachiopods and carbonate rocks as proxies for coeval seawater and palaeotemperature. *Palaeogeography Palaeoclimatology Palaeoecol.* 226, 287–306. doi: 10.1016/j.palaeo.2005.05.018

Kustatscher, E., Cittert, V. K-V. J. H. A., and & Roghi, G. (2010). Macrofloras and palynomorphs as possible proxies for palaeoclimatic and palaeoecological studies: A case study of Kuehwiesenkopf/Monte Prà della Vacca (Olang dolostones, N-Italy). *Palaeogeography Palaeoclimatology Palaeoecol.* 290, 71–80. doi: 10.1016/j.palaeo.2009.07.001

Kustatscher, E., Manfrin, S., Mietto, P., Posenato, R., and Roghi, G. (2006). New biostratigraphic data on Anisian (Middle Triassic) palynomorphs from the dolostones, Italy. *Rev. Palaeobotany Palynology* 140, 79–90. doi: 10.1016/j.revpalbo.2006.03.003

Kustatscher, E., and Roghi, G. (2006). Anisian palynomorphs from the Dont Formation of Kühwiesenkopf — Monte Prà della Vacca section (Braies dolostones, Italy). *Micropalaeontology* 52, 223–244. doi: 10.2113/gsmicropal.52.3.223

Land, L. S. (1983). "The application of stable isotopes to studies of the origin of dolostone and to problems of diagenesis of clastic sediments," in *Stable isotopes in sedimentary geology*, vol. 10 . Eds. M. A. Arthur, T. F. Anderson, I. R. Kaplan, J. Veizer and L. S. Land (SEPM Short Course Notes). (Berlin, Heidelberg: Springer) 4 - 1–44-22. doi: 10.1007/BFb0009861

Land, L. S. (1992). "The dolostone problem: stable and radiogenic isotope clues," in *Isotopic signature of sedimentary records. Lecture notes in earth science*, Berlin, Heidelberg: Springer. vol. 43 . Eds. N. Clauer and S. Chaudhuri, 49–68.

Lawrence, M. O., and Graham, A. S. (2012). The Neoproterozoic oxygenation event: Environmental perturbations and biogeochemical cycling. *Earth-Science Rev.* 110, 26–57. doi: 10.1016/j.earscirev.2011.09.004

Lehrmann, D. J., Minzoni, M., Enos, P., Yu, Y. Y., Wei, J. Y., Li, R. X., et al. (2009). Triassic depositional history of the Yangtze platform and Great Bank of Guizhou in the Nanpanjiang Basin of South China. *J. Earth Sci. Environ.* 31, 344–367.

Lerman, A., Imboden, D. M., and Gat, J. R. (1995). *Physics and chemistry of lakes* (Berlin: Springer-Verlag).

Li, M. S., Huang, C. J., Hinnov, L., Chen, W. Z., Ogg, J., and Tian, W. (2018). Astrochronology of the Anisian stage (Middle Triassic) at the Guandao reference section, South China. *Earth Planetary Sci. Lett.* 482, 591–606. doi: 10.1016/j.epsl.2017.11.042

Li, M. S., Ogg, J., Zhang, Y., Huang, C. J., Hinnov, L., Chen, Z. Q., et al. (2016). Astronomical-cycle scaling of the end-Permian extinction and the Early Triassic Epoch of South China and Germany. *Earth Planetary Sci. Lett.* 441, 10–25. doi: 10.1016/j.epsl.2016.02.017

Li, M. S., Wignall, P. B., Dai, X., Hu, M. Y., and Song, H. J. (2021). Phanerozoic variation in dolostone abundance linked to oceanic anoxia. *Geology* 49, 698–702. doi: 10.1130/G48502.1

Li, D. D., Zhang, X. L., Zhang, X., Zhu, H., Peng, S. C., Sun, L. L., et al. (2020). A paired carbonate–organic δ13C approach to understanding the Cambrian Drumian carbon isotope excursion (DICE). *Precambrian Res.* 349, 105503. doi: 10.1016/j.precamres.2019.105503

Luan, G. Q., Lin, C. Y., Azmy, K., Fu, L. Y., Dong, C. M., Liu, H. C., et al. (2024). Marine anoxia events across the upper Cambrian (stage 10) of eastern Gondwana: Implications from paleoenvironmental geochemical proxies. *Mar. Petroleum Geology* 164. doi: 10.1016/j.marpetgeo.2024.106813

Luo, G. M. (2011). *Microbial geological processes and the associated biogeochemical cycles of carbon, nitrogen, and sulfur during the Permian–Triassic crisis interval. (Ph.D. dissertation)* (Wuhan: China University of Geosciences), 202.

Luo, G. M., Algeo, T. J., Huang, J., et al. (2014). Vertical $\delta^{13}C_{org}$ gradients record changes in planktonic microbial community composition during the end-Permian mass extinction. *Palaeogeography Palaeoclimatology Palaeoecol.* 396, 119–131. doi: 10.1016/j.palaeo.2014.01.006

Luo, M., Chen, Z. Q., Zhao, L., et al. (2014). Early Middle Triassic stromatolites from the Luoping area, Yunnan Province, Southwest China: Geobiologic features and environmental implications. *Palaeogeography Palaeoclimatology Palaeoecol.* 412, 124–140. doi: 10.1016/j.palaeo.2014.07.028

Luo, G. M., Kump, L. R., Wang, Y. B., et al. (2010). Isotopic evidence for an anomalously low oceanic sulphate concentration following end-Permian mass extinction. *Earth Planet. Sci. Lett.* 300, 101–111. doi: 10.1016/j.epsl.2010.09.041

Luo, G. M., Wang, Y., Grice, K., Kershaw, S., Algeo, T. J., Ruan, X. Y., et al. (2013). Microbial composition in microbialites during the Late Permian ecological crisis at the Cili section, South China: evidence from lipid biomarkers. *Glob. Planet. Change* 105, 36–51. doi: 10.1016/j.gloplacha.2012.11.015

McLennan, S. M. (2001). Relationships between the trace element composition of sedimentary rocks and upper continental crust. *G-cubed* 2. doi: 10.1029/2000GC000109

Moei, Y., Kazutaka, Y., Kentaro, N., Minoru, I., and Yasuhiro, K. (2020). Geochemical features of redox-sensitive trace metals in sediments under oxygen-depleted marine environments. *Minerals* 10, 1021. doi: 10.3390/min10111021

Nédélec, A., Affaton, P., France-lanord, C., Charrière, A., and & Alvaro, J. (2007). Sedimentology and chemostrati-graphy of the Bwipe Neoproterozoic cap dolostones (Ghana, Volta Basin): A record of microbial activity in a peritidal environment. *C. R. Geosci.* 339, 223–239. doi: 10.1016/j.crte.2005.06.002

Okafor, M., and Azmy, K. (2024). Redox conditions across the Upper Cambrian of eastern Laurentia: Implications from geochemical proxies. *Palaeogeography Palaeoclimatology Palaeoecol.* 637. doi: 10.1016/j.palaeo.2023.111978

Payne, J. L., and Kump, L. R. (2007). Evidence for recurrent Early Triassic massive volcanism from quantitative interpretation of carbon isotope fluctuations. *Earth Planetary Sci. Lett.* 256, 264–277. doi: 10.1016/j.epsl.2007.01.034

Payne, J. L., Lehrmann, D. J., Wei, J., Orchard, M. J., Schrag, D. P., and Knoll, A. H. (2004). Large perturbations of the carbon cycle during recovery from the end-Permian extinction. *Science* 305, 506–509. doi: 10.1126/science.1097023

Pei, Y., Hagdorn, H., Voigt, T., Duda, J. P., and Reitner, J. (2022). Palaeoecological implications of lower-middle triassic stromatolites and microbe-metazoan build-ups in the germanic basin: insights into the aftermath of the permian–triassic crisis. *Geosciences* 12, 133. doi: 10.3390/geosciences12030133

Reinhard, C. T., Planavsky, N. J., Gill, B. C., Ozaki, K., Robbins, L. J., Lyons, T. W., et al. (2017). Evolution of the global phosphorus cycle. *Nature* 541, 386–389. doi: 10.1038/nature20772

Retallack, G. J. (2013). Permian and Triassic greenhouse crises. *Gondwana Res.* 24, 90–103. doi: 10.1016/j.gr.2012.03.003

Retallack, G. J., Sheldon, N. D., Carr, P. F., Fanning, M., Thompson, C. A., Williams, M. L., et al. (2011). Multiple Early Triassic greenhouse crises impeded recovery from Late Permian mass extinction. *Palaeogeography Palaeoclimatology Palaeoecol.* 308, 233–251. doi: 10.1016/j.palaeo.2010.09.022

Riding, R. (2000). Microbial carbonates: The geological record of calcified bacterial-algal mats and biofilms. *Sedimentology* 47, 179–214. doi: 10.1046/j.1365-3091.2000.00003.x

Robacio, L. G., Azmy, K., Guéguen, B., and Claret, F. (2024). Paleoenvironmental variations during the Late Cambrian: Implications from Zn isotopes, I/(Ca+Mg) ratios, and other elemental proxies. *Mar. Petroleum Geology* 165. doi: 10.1016/j.marpetgeo.2024.106817

Sahney, S., and Benton, M. J. (2008). Recovery from the most profound mass extinction of all time. *Proc. R. Society Ser. B* 275, 759–765. doi: 10.1098/rspb.2007.1370

Schoepfer, S. D., Shen, J., Wei, H. Y., Tyson, R. V., Ingall, E., Algeo, T. J., et al. (2015). Total organic carbon, organic phosphorus, and biogenic barium fluxes as proxies for paleomarine productivity. *Earth Sci. Rev.* 149, 23–52. doi: 10.1016/j.earscirev.2014.08.017

Shen, J., Schoepfer, S. D., Feng, Q., Zhou, L., Yu, J., Song, H., et al. (2015). Marine productivity changes during the end-Permian crisis and Early Triassic recovery. *Earth-Science Rev.* 149, 136–162. doi: 10.1016/j.earscirev.2014.11.002

Śliwiński, M. G., Whalen, M. T., and Day, J. (2010). Trace element variations in the Middle Frasnian Punctata Zone (Late Devonian) in the western Canada sedimentary basin—Changes in oceanic bioproductivity and paleoredox spurred by a pulse of terrestrial afforestation? *Geologica Belgica* 4, 459–482.

Song, H. J., Wignall, P. B., and Tong, J. (2015). Integrated Sr isotope variations and global environmental changes through the Late Permian to early Late Triassic. *Earth Planetary Sci. Lett.* 424, 140–147. doi: 10.1016/j.epsl.2015.05.035

Stanley, S. M. (2009). Evidence from ammonoids and conodonts for multiple Early Triassic mass extinctions. *Proc. Natl. Acad. Sci. United States America* 106, 15264–15267.

Stefani, M., Furin, S., and Gianolla, P. (2010). The changing climate framework and depositional dynamics of Triassic carbonate platforms from the Dolomites. *Palaeogeography Palaeoclimatology Palaeoecol.* 290, 43–57. doi: 10.1016/j.palaeo.2010.02.018

Sun, Y., Joachimski, M. M., Wignall, P. B., Yan, C. B., Chen, Y. L., Jiang, H. S., et al. (2012). Lethally hot temperatures during the Early Triassic greenhouse. *Science* 338, 366–370. doi: 10.1126/science.1224126

Swart, P. K. (2015). The geochemistry of carbonate diagenesis: The past, present and future. *Sedimentology* 62, 1233–1304. doi: 10.1111/sed.12205

Swart, P. K., and Eberli, G. (2005). The nature of the δ13C of periplatform sediments: implications for stratigraphy and the global carbon cycle. *Sedimentary Geology* 175, 115–129. doi: 10.1016/j.sedgeo.2004.12.029

Tong, J. N., Chu, D. L., Liang, L., Shu, W. C., Song, H. J., Song, T., et al. (2021). Lithostratigraphic subdivision and correlation of the Triassic in China. *J. Stratigraphy* 45, 340–363.

Tribovillard, N., Algeo, T. J., Lyons, T., and Riboulleau, A. (2006). Trace metals as paleoredoxand paleoproductivity proxies: an update. *Chem. Geology* 232, 12~32.

Tripathy, G. R., Singh, S. K., and Ramaswamy, V. (2014). Major and trace element geochemistry of Bay of Bengal sediments: implications to provenances and their controlling factors. *Paleogeography Paleoclimatology Paleoecology* 397, 20–30. doi: 10.1016/j.palaeo.2013.04.012

Trotter, J. A., Williams, I. S., Barnes, C. R., Lécuyer, C., and Nicoll, R. S. (2008). Did cooling oceans trigger Ordovician biodiversification? Evidence from conodont thermometry. *Science* 321, 550–554. doi: 10.1126/science.1155814

Veizer, J. (1983a). Chemical diagenesis of carbonates: Theory and application of trace element technique, in M. A. Arthur, ed. *Stable isotopes sedimentary geology: SEPM Short Course Notes* 10, 3.1–3.100.

Veizer, J., Ala, D., Azmy, K., Bruckschen, P., Buhl, D., Bruhn, F., et al (1983b). Trace elements and isotopes in sedimentary carbonates. *Rev. Mineralogy Geochemistry* 11, 265–299. doi: 10.1515/9781501508134

Veizer, J., et al. (1999). 87Sr/86Sr, d13C and d18O evolution of Phanerozoic seawater: Chemical Geology. *Chemical Geology* 161, 59–88. doi: 10.1016/S0009-2541(99)00081-9

Wang, L., and Azmy, K. (2020). Paleoenvironmental changes in slope carbonates across the late Cambrian-early Ordovician in western Newfoundland. *Geol. J.* 55, 1–13.

Wang, H., Yong, Z. Q., Song, J. M., et al. (2023). Microbialite textures and their geochemical characteristics of middle triassic dolostones, sichuan basin, China. *Processes* 11, 1541. doi: 10.3390/pr11051541

Whiteside, J. H., and Ward, P. D. (2011). Ammonoid diversity and disparity track episodes of chaotic carbon cycling during the early Mesozoic. *Geology* 39, 99–102. doi: 10.1130/G31401.1

Wignall, P. B., and Twitchett, R. J. (1996). Oceanic anoxia and the end Permian mass extinction. *Science* 272, 1155–1158. doi: 10.1126/science.272.5265.1155

Wignall, P. B., Zonneveld, J. P., Newton, R. J., et al. (2007). The end Triassic mass extinction record of Williston Lake, British Columbia. *Palaeogeogr. Palaeoclimatol. Palaeoecol.* 253, 385–406. doi: 10.1016/j.palaeo.2007.06.020

Xia, W., Chen, A., Azmy, K., et al. (2023). A pilot study of upper Yangtze shallow-water carbonates of the Paibian global marine euxinia: Implications for the late Cambrian SPICE event. *Mar. Petroleum Geology* 150, 106146. doi: 10.1016/j.marpetgeo.2023.106146

Yang, J., Cawood, P. A., Du, Y. D., Condon, J., Yan, J., Liu, J., et al. (2018). Early Wuchiapingian cooling linked to Emeishan basaltic weathering? *Earth Planetary Sci. Letters v. 492* p, 102–111. doi: 10.1016/j.epsl.2020.116074

Yang, J., Cawood, P. A., Du, Y., Feng, B., and Yan, J. (2014). Global continental weathering trends across the Early Permian glacial to postglacial transition: Correlating high- and lowpaleolatitude sedimentary records: Geology, v. *42* p, 835–838. doi: 10.1016/j.epsl.2018.04.004

Yin, H. F., Zhang, K., Tong, J., Yang, Z. Y., and Wu, S. (2001). The Global Strato type Section and Point (GSSP) of the Permian-Triassic boundary. *Episodes* 24, 102–114.

Zhao, L. S., Chen, Y. L., Chen, Z. Q., et al. (2013). Uppermost Permian to Lower Triassic conodont zonation from Three Gorges area, South China. *Palaios* 28, 523–540. doi: 10.2110/palo.2012.p12-107r

Zhou, W., Algeo, T. J., Ruan, X., et al. (2017). Expansion of photic-zone euxinia during the Permian–Triassic biotic crisis and its causes: Microbial biomarker records. *Palaeogeography Palaeoclimatology Palaeoecol.* 474, 140–151. doi: 10.1016/j.palaeo.2016.06.027

Zhu, B., Guo, T., Liu, C., et al. (2023). Coastal upwelling and redox variations in the northwestern Tarim Basin (northwest China) during the Middle-Late Ordovician: Implication for paleo-depositional conditions of the organic matter enrichment in the Saergan Formation. *Front. Earth Sci.* 11. doi: 10.3389/feart.2023.1321488